Simultaneous two-photon imaging of intracellular chloride concentration and pH in mouse pyramidal neurons in vivo

Sebastian Sulis Sato[a,1], Pietro Artoni[a,1], Silvia Landi[a,1], Olga Cozzolino[a,1], Riccardo Parra[a], Enrico Pracucci[a], Francesco Trovato[a], Joanna Szczurkowska[b], Stefano Luin[a], Daniele Arosio[c,d], Fabio Beltram[a], Laura Cancedda[b], Kai Kaila[e], and Gian Michele Ratto[a,2]

[a]National Enterprise for Nanoscience and Nanotechnology (NEST), Istituto Nanoscienze Consiglio Nazionale delle Ricerche (CNR) and Scuola Normale Superiore Pisa, 56127 Pisa, Italy; [b]Neuroscience and Brain Technologies Department, Istituto Italiano di Tecnologia, 16163 Genoa, Italy; [c]Institute of Biophysics, National Research Council and Bruno Kessler Foundation, 38122 Trento, Italy; [d]Centre for Integrative Biology, University of Trento, 38122 Trento, Italy; and [e]Department of Biosciences and Neuroscience Center (HiLife), University of Helsinki, 00014 Helsinki, Finland

Intracellular chloride ($[Cl^-]_i$) and pH (pH_i) are fundamental regulators of neuronal excitability. They exert wide-ranging effects on synaptic signaling and plasticity and on development and disorders of the brain. The ideal technique to elucidate the underlying ionic mechanisms is quantitative and combined two-photon imaging of $[Cl^-]_i$ and pH_i, but this has never been performed at the cellular level in vivo. Here, by using a genetically encoded fluorescent sensor that includes a spectroscopic reference (an element insensitive to Cl^- and pH), we show that ratiometric imaging is strongly affected by the optical properties of the brain. We have designed a method that fully corrects for this source of error. Parallel measurements of $[Cl^-]_i$ and pH_i at the single-cell level in the mouse cortex showed the in vivo presence of the widely discussed developmental fall in $[Cl^-]_i$ and the role of the K-Cl cotransporter KCC2 in this process. Then, we introduce a dynamic two-photon excitation protocol to simultaneously determine the changes of pH_i and $[Cl^-]_i$ in response to hypercapnia and seizure activity.

fluorescent indicators | neurodevelopment | neuronal inhibition | bumetanide | NKCC1

Intracellular ion concentrations are controlled by plasmalemmal transporters and channels, which generate and dissipate ionic electrochemical gradients, respectively (1). In recent years, regulation of the intracellular Cl^- concentration ($[Cl^-]_i$) in neurons has attracted lots of attention, because it is the main ion that carries current across $GABA_A$ (and also, glycine) receptors. Changes in $[Cl^-]_i$ exert an immediate effect on the reversal potential of GABAergic currents (E_{GABA}) and, thereby, on the properties of $GABA_A$ receptor-mediated transmission (2–4). The "ionic plasticity" of GABAergic signaling involves not only the passive flux of Cl^- ions through membrane channels but also, a number of ion transporters that regulate $[Cl^-]_i$. Furthermore, this mechanism is under the control of intracellular signaling cascades that regulate the expression patterns as well as functional properties of ion transporters and channels (5, 6). With regard to long-term ionic modulation of GABAergic transmission, a case in point is the decrease in $[Cl^-]_i$ that is generally thought to take place during maturation of most central neurons. According to this widely accepted scenario, the Na-K-2Cl cotransporter NKCC1 accumulates Cl^- in immature neurons, thereby promoting depolarizing GABA responses (3, 7–9), which is followed by developmental upregulation of the neuron-specific K-Cl cotransporter KCC2 that is required for the generation of classical hyperpolarizing inhibitory postsynaptic potentials (IPSPs) (10).

A wealth of electrophysiological evidence dating back to the work in vivo by Eccles and coworkers (11) has provided evidence for active regulation of $[Cl^-]_i$ in mammalian central neurons and its crucial effect on the driving force of Cl^- in inhibitory synapses (1). However, thus far, there are no direct data on neuronal $[Cl^-]_i$ measured in vivo at the single-cell level in the living brain, and for

instance, the very existence of the developmental shift in $[Cl^-]_i$ described above has been intensely debated (12) because of the lack of such measurements. Moreover, it has been postulated that, in some diseases, such as autism and Down syndrome, the ion-regulatory mechanisms underlying $GABA_A$ signaling do not properly mature (12–16), and E_{GABA} can revert from hyperpolarizing to depolarizing in mature neurons as has been reported for epilepsy and stroke (3, 17–19). Thus, a technique for monitoring $[Cl^-]_i$ in vivo would substantially add to our understanding of Cl^--regulatory mechanisms and their roles in brain development, plasticity, and disease. The need for an imaging-based method has long been recognized, and several fluorescent sensors have been designed for this purpose (20); however, no reliable data have been obtained so far.

In this study, we exploit a probe, LSSmClopHensor, formed by the fusion of a Cl^-- and pH-sensitive GFP mutant (E^2GFP) with an ion-insensitive red fluorescent protein, LSSmKate2 (21). The fact that this construct reports changes in both $[Cl^-]_i$ and intracellular pH (pH_i) is highly advantageous, because regulation of Cl^- and H^+/HCO_3^- is tightly linked via common transport (22, 23) and channel (3) mechanisms. Furthermore, pH_i is also a powerful ionic modulator of neuronal excitability (22, 24–26).

Significance

The control of intracellular Cl^- and pH plays a crucial role in several neuronal functions, and the study of these processes would be helped by tools for their noninvasive optical measurement in vivo. In this study, we have performed combined measurements of Cl^- and pH of individual pyramidal neurons by means of in vivo two-photon imaging, and we provide direct experimental demonstration for the presence of the postnatal developmental shift to lower intraneuronal Cl^-. Moreover, we introduce an approach for dynamic and simultaneous monitoring of intraneuronal Cl^- and pH in vivo. These methods will open a window for the study of the roles of intraneuronal pH and Cl^- in neuronal signaling, plasticity, and disease.

We determined the two-photon spectroscopic properties of LSSmClopHensor as a function of pH and [Cl⁻]. Then, we show that the propagation of both excitation light and emitted fluorescence in the brain is strongly dependent on wavelength, which can cause large errors, even in ratiometric measurements of $[Cl^-]_i$ and pH_i. By using the red fluorescent protein, LSSmKate, as an invariant reference, we are able to fully correct for this source of error. The validity of this correction was independently verified by fluorescence lifetime imaging microscopy (FLIM) measurements of pH_i, which notably, are not affected by scattering effects in brain tissue. Thus, our imaging technique allowed for direct and simultaneous measurements of neuronal $[Cl^-]_i$ and pH_i at the single-cell level in vivo. We present here direct evidence for the developmental decrease in $[Cl^-]_i$ and of the involvement of NKCC1 in the maintenance of high $[Cl^-]_i$ in immature neurons. Finally, we combined a methodology for dynamic in vivo imaging with local field potential (LFP) recordings to show the interplay between changes of network activity and the modulation of neuronal $[Cl^-]_i$ and pH_i in response to hypercapnia and seizure.

Results

Two-Photon Spectral Properties of LSSmClopHensor: Dependency on pH and Chloride. We used the Cl⁻ and pH sensor LSSmClopHensor (21) formed by the fusion of E²GFP (27) and of the red fluorescent protein, LSSmKate2 (28) (Fig. 1A). Since the excitation spectrum of E²GFP depends on pH and because its fluorescence is quenched on Cl⁻ binding, E²GFP provides a pH- and Cl-dependent signal (29). In contrast, LSSmKate2 is insensitive to pH and Cl⁻, thus providing a ratiometric reference.

We characterized the two-photon excitation spectra of LSSmClopHensor and its dependency on pH and Cl⁻. We calibrated the purified sensor protein in aqueous solutions, where we

could control temperature, pH, and Cl⁻ concentration with great precision. Furthermore, given the fast diffusion of the protein in solution, these spectra are unaffected by photobleaching and have an optimal signal to noise ratio. Fig. 1B shows that the excitation of LSSmKate2 is independent of pH after correction for bleed through and that the E²GFP spectra display a well-defined isosbestic point at about 910 nm (details are in *Materials and Methods*, and Figs. S1 and S2 show raw data). The E²GFP spectrum at an arbitrary pH is given by the linear combination of the protonated and deprotonated spectra, and the relative contributions of these terms are used to compute pH_i (Fig. 1 C and D).

LSSmClopHensor is a double-ratiometric indicator both in excitation and emission that requires two steps to complete a measurement. First, pH_i is determined by the excitation spectra of E²GFP. Although it is enough to collect the fluorescence at only two different excitation wavelengths, it is possible to obtain a more reliable estimate of pH_i by sampling the excitation spectra at several wavelengths. Second, since the sensor exploits the quenching of E²GFP fluorescence on Cl⁻ binding (29), increases of Cl⁻ led to a drop of E²GFP fluorescence relative to LSSmKate2 (Fig. 1E), and the ratiometric analysis of the emitted fluorescence provides the Cl⁻ measurement (details are in *Materials and Methods*).

Properties of LSSmClopHensor Expressed in Vivo. In utero electroporation (30, 31) applied at embryonic day 15.5 led to the transfection of layer 2/3 pyramidal neurons of the visual cortex as shown in a postnatal day (P) 32 mouse (Fig. 2 A and B). A spectral sequence is obtained by imaging the same cells at different excitation wavelengths. Each image in Fig. 2C has been obtained at the indicated wavelength by in vivo imaging in a P10 mouse. The quantification of the raw fluorescence of five cells (Fig. 2D) is shown in Fig. 2E, while Fig. 2F shows the effects of correction for bleed through (Eq. 6 and Fig. S1C).

Fig. 1. Two-photon spectra of LSSmClopHensor in aqueous solution. (A) Schematic structure of the sensor. (B) Excitation spectra of the E²GFP and LSSmKate2 components of LSSmClopHensor at different levels of pH at 24 °C. Data have been corrected for bleed through and normalized using the peak of the LSSmKate2 emission. The nonlabeled spectra of E²GFP have been obtained at pH 6.4, 6.8, 6.9, 7.1, 7.2, 7.4, and 7.6. The excitation spectrum of LSSmKate2 is pH-insensitive: *Lower* shows the normalized difference (percentage) between the spectra obtained at pH values of 6, 7, and 8, with the mean spectrum averaged for all pH levels. (C) Linear decomposition of the spectrum obtained at pH 7.0 (green symbols) on the spectra obtained at pH 6.0 and 8.0 (thin red and blue lines, respectively). The two components are represented by the thick red and blue curves, respectively, and their sum is the line running through the experimental points. (D) The color-coded circles represent the corresponding coefficients in the linear decomposition of the spectra of the set of calibration solutions shown in B. The ratio between the components provides the angle θ, which is specific for each value of pH. The error bars, computed from the fit residues (*Supporting Information*), are contained within the symbol size. (E) Chloride determines the quenching of the E²GFP signal as shown by the loss of fluorescence measured at the isosbestic point. Green circles and line of best fit show the ratio of the fluorescence excited at 910 nm in the green and red channels (normalized to 1 at the maximum) as a function of chloride concentration. The apparent chloride K_d depends on pH, because

chloride binds only to protonated E²GFP. Dashed lines are calculated for pH 6.0 and 8.0. Spectra have been obtained from three different samples, and each has been analyzed at three different temperatures (Fig. S2).
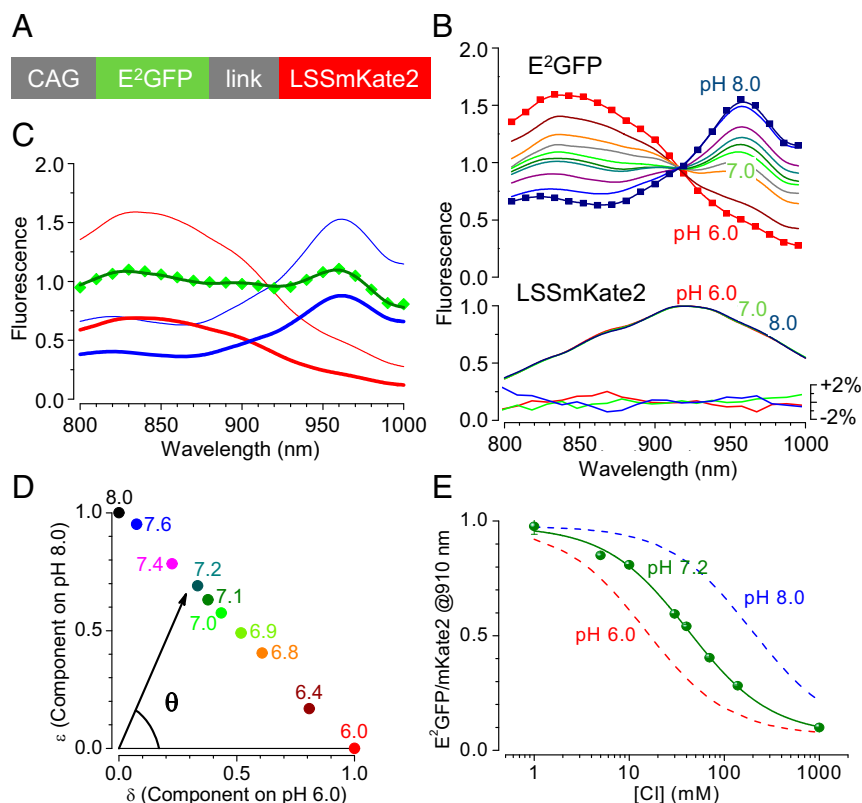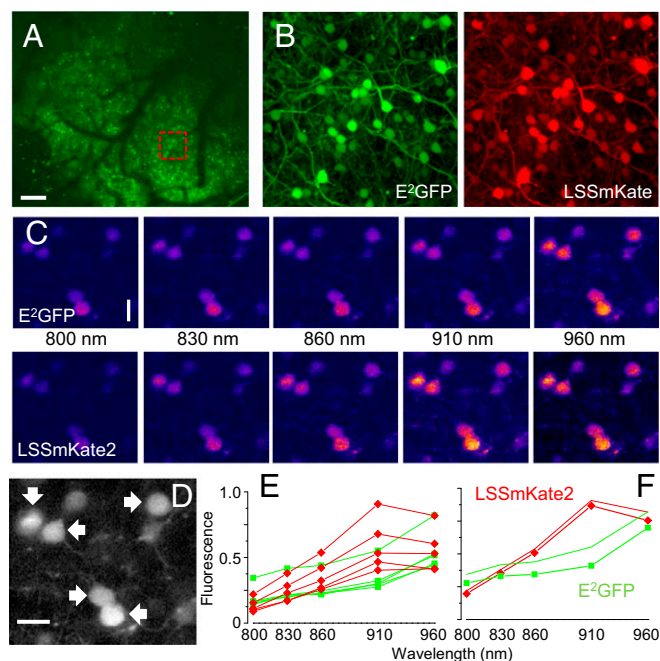
Fig. 2. Expression and spectra of LSSmClopHensor in vivo after transfection by in utero electroporation. (*A*) Two-photon wide-field imaging of the visual cortex in a P32 mouse. The image is a mosaic showing the entire extension of a 2-mm-wide craniotomy (stack depth: 250 μm; objective 10×, 0.3 N.A.; excitation at 910 nm). (Scale bar: 200 μm.) (*B*) Magnified image of the boxed area from *A* showing the E²GFP (green) and LSSmKate2 (red) fluorescence after correction for bleed through. Field width is 200 μm; objective is 60× and 1.00 N.A. A γ transform (γ = 0.5) was applied to *A* and *B* to improve visualization of dendrites. (*C*) Image sequence obtained at the indicated wavelengths in a P10 mouse. (Scale bar: 20 μm.) (*D* and *E*) Quantification of the raw fluorescence of the five cell bodies indicated by the arrows in *D*. Data have only been corrected for flat-field illumination and background. (Scale bar: *D*, 20 μm.) (*F*) Spectra of one cell after correction for bleed through (symbols connected by lines) compared with the raw data without bleed-through correction (lines). Fluorescence intensity shown in arbitrary units.

We verified that the product of expression of the plasmid was an intact E²GFP-LSSmKate2 fusion protein by performing two independent controls based on in vivo fluorescence recovery after photobleaching and on the study of fluorescence fluctuations (32) (Fig. S3).

Effects of Brain Tissue on Sensor Spectroscopy. Steady-state [Cl⁻]ᵢ was studied in vivo by acquiring images at several wavelengths under a constant power at the brain surface (33) as shown in Fig. 2 *C–E*. Spectra were corrected for field illumination and bleed through and were normalized to the photon flux density used at each wavelength before data analysis (*Materials and Methods*). Despite the above corrections, the spectra observed in vivo showed a clear mismatch with regard to the calibrations that was not caused by bleaching occurring during the scan (Fig. S4). Owing to this mismatch, the calculated values of pHᵢ and [Cl⁻]ᵢ turned out to be very dispersed. We hypothesized that imaging was affected by wavelength-dependent absorption and scattering of excitation and emission light by brain tissue (34). To test this idea, we used mice expressing YFP in a sparse population of cortical pyramidal cells (line H in ref. 35). Fig. 3*A* shows the ratio of the fluorescence emitted by YFP when excited at 960 and 910 nm (F_{960} and F_{910}, respectively) normalized to the ratio observed in a monolayer culture of HEK293T cells. The color-coded transverse section shows that, as the imaging depth increased, F_{910} decreased compared with F_{960}, thus indicating a progressive loss of two-photon excitation at the focal plane with decreasing wavelength (Fig. 3*B*). This observation

implies that also the emitted fluorescence must undergo some extinction while propagating from the imaging plane to the brain surface, with the green fluorescence experiencing more loss than the red one. We obtained a quantitative assessment of this effect in the YFP mice. When measuring the fluorescence of YFP expressed in cultures, the emission spectrum was not altered by extinction, and the fluorescence of YFP was distributed in the green and red channels with a ratio R/G = 0.116 (SD = 0.006, n = 10 cells). Next, we recorded the fluorescence in YFP mice in the red and green channels and computed the R/G ratio at various focal depths (see Fig. S5 for the YFP emission spectrum). As expected, the ratio R/G changed with depth, as shown in Fig. 3*C*, which reports qualitatively the R/G ratio normalized to the R/G value observed in culture. Fig. 3*D* shows a quantification of the red shift of detected fluorescence with increasing depth.

Next, we examined whether, for a given focal plane, we could establish a relationship between excitation scattering/absorption and emission extinction. Fig. 3*E* shows the correlation between these two effects as quantified by the measured Δ–γ pairs at different depths. Δ(z) yields the relative loss of fluorescence excited at 960 and 910 nm as defined by

$$\Delta(z) = \frac{YFP_{960}(z)}{YFP_{910}(z)} \frac{YFP_{910}(0)}{YFP_{960}(0)}, \quad [1]$$

where the subscripts indicate the excitation wavelength, and z indicates the imaging depth. Depth 0 corresponds to tissue surface where no scattering occurs, and Δ = 1 implies that there is no wavelength-dependent loss of excitation power. γ(z) is defined by

$$\gamma(z) = \frac{R_{YFP}(z)}{G_{YFP}(z)} \frac{G_{YFP}(0)}{R_{YFP}(0)}, \quad [2]$$

where z is the imaging depth. The value of γ(z) is equal to 1 in the absence of differential extinction of the fluorescence detected in the R and G channels. Fig. 3*E* shows that there is a linear relationship between the extinction of emission and the loss of excitation and that this relationship is similar in cortical neurons of different mice. Based on this finding, if Δ(z) is known, the parameter for differential emission extinction, γ, can be readily estimated using the empirical relationship:

$$\gamma = 1 + \mu(\Delta(z) - 1), \quad [3]$$

with μ = 0.40 ± 0.016 (n = 66 cells from six mice) (Fig. 3*E*).

In Vivo Measurements of pHᵢ and [Cl⁻]ᵢ. Fig. 4*A* illustrates the computation of steady-state pHᵢ and [Cl⁻]ᵢ. After calibration of the images (*Supporting Information*), the fluorescence within the cell body outline was measured and corrected for bleed through to obtain the excitation spectra of E²GFP and LSSmKate2. As explained above, the spectra obtained at a given depth in the tissue must be corrected for loss of absorption/scattering before computing the pH values. We performed this correction knowing that $R_{*z}(\lambda)$ (the LSSmKate2 spectrum obtained in vivo at depth z) is not affected by pH and Cl⁻. Therefore, any divergence between $R_{*z}(\lambda)$ and the LSSmKate2 spectra must be caused by wavelength-dependent loss of excitation. Thus, we computed the correction factors φz(λ) defined as

$$\varphi_z(\lambda) = \frac{R_{*0}(\lambda)}{R_{*z}(\lambda)}, \quad [4]$$

where $R_{*0}(\lambda)$ indicates the LSSmKate2 excitation spectrum corrected for bleed through at depth 0. We used this set of factors to correct the E²GFP spectrum:

Fig. 3. The recorded excitation and emission spectra of intracellular fluorescence are altered by the depth of imaging. (*A*) Imaging of cortical neurons in a YFP-expressing mouse shows the wavelength-dependent loss of excitation in vivo. The reconstructed transverse section depicts the ratio of the fluorescence emitted in response to excitation at 960 and 910 nm. The ratio has been normalized to the value measured at zero absorption/scattering (brain surface), and as the imaging depth increases, excitation at 960 nm is less attenuated. (Scale bar: 50 μm.) (*B*) Excitation spectra of YFP imaged at different depths in the cortex of one adult YFP-expressing mouse. As a zero distortion reference, the spectrum of YFP recorded in HEK cells is also shown. Spectra have been normalized to the fluorescence measured at 1,000 nm to allow for an easier comparison. This normalization shows that, at increasing imaging depth, shorter wavelengths are transmitted more poorly with a consequent decrement of fluorescence. Similar results on neurons in vivo were obtained in five additional mice. (*C*) Effects of imaging depth on the color of recorded fluorescence. The image is a reconstructed transverse section of neurons from a YFP-expressing mouse showing the ratio of the fluorescence recorded in the G and R channels. In HEK cells, the emitted fluorescence is distributed between the R and G channels with a ratio of 0.116 (SD = 0.116, n = 10). With increasing depth, the green fluorescence undergoes more extinction than the red, and the ratio decreases to 1/0.38. (Scale bar: 50 μm.) (*D*) Quantification of the progressive red shift of detected fluorescence γ with imaging depth. Data collected from neurons (n = 290) of six YFP-expressing adult mice. (*E*) Correlation between differential excitation scattering (parameterized by Δ) and fluorescence red shift γ ($R^2 = 0.73$).
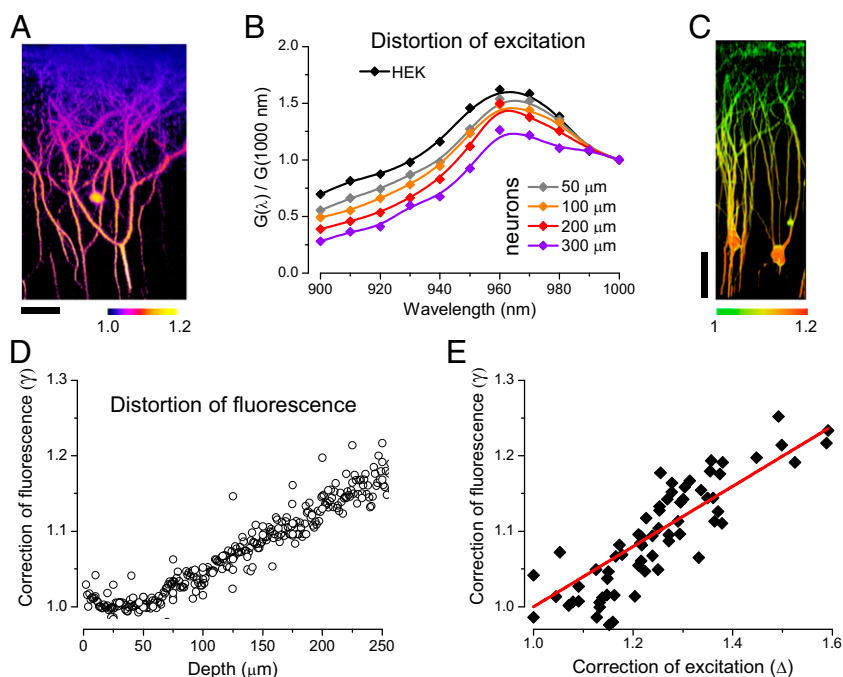
$$G^{\cdot}(\lambda) = G_{*_z}(\lambda)\varphi_z(\lambda), \qquad [5]$$

where $G_{*_z}(\lambda)$ indicates the E^2GFP spectrum corrected for bleed through at depth z. Fig. 4*A* shows that the effect of excitation loss on the sensor spectra was very strong. After computation of pH_i, the fit residue R provided a readout of the quality of the pH estimate. $[Cl^-]_i$ was then computed using the correction for the extinction of emission (Eq. 3) and Eqs. 7–12. Fig. 4*B* compares the residues R, pH_i, and $[Cl^-]_i$ for each neuron acquired in an imaging run at various depth in the tissue. We computed these parameters on the raw data, after correction for bleed through, and after correction for excitation scattering and extinction of emission. The dispersion of the pH and $[Cl^-]_i$ estimates and the magnitude of R decreased radically after these corrections. Fig. 4 *C* and *D* shows the pH_i and $[Cl^-]_i$ maps and the uncertainties of the ion measurements (details are in *Supporting Information*) at each pixel within the outlines of the cell bodies. Although we had verified that the effect of photobleaching on the spectroscopic data was negligible (Fig. S4), during acquisition of the spectroscopic series, the wavelength presentation was randomized to exclude any bias caused by bleaching. Importantly, this procedure was validated by measuring the fluorescence lifetime of LSSmClopHensor as an alternative method to estimate pH_i, since this approach is independent of excitation distortion (Fig. S6).

Developmental Decrease of the Intraneuronal Chloride Concentration.
Next, we exploited our technical approach to address the question whether a developmental decrease in $[Cl^-]_i$, akin to that shown in numerous studies in vitro, also takes place during the maturation of cortical neurons in vivo. We studied mice at three stages of development [P4–P5 (n = 9 mice, 182 neurons), P8–P10 (n = 8 mice, 512 neurons), and P18–P51 (n = 5 mice, 226 neurons)] under light urethane anesthesia. From the excitation spectra for E^2GFP and LSSmKate2, we obtained the Cl^- and pH maps, as shown in Fig. 5 *A* and *B*. This analysis was limited to the cell bodies, because most of the corresponding in vitro data are based on somatic measurements and also because the cell body provides

a better signal-to-noise ratio for ion imaging than the dendrites. While no large age-dependent change in neuronal pH_i was detected as shown by the median and interquartile range (IQR; pH_i IQR 7.11–0.27, 7.17–0.23, and 7.16–0.25 at P4–P5, P8–P10, and P18–P51, respectively) (Fig. 5*C*), a robust developmental shift in $[Cl^-]_i$ was clearly evident among the three age groups. The median level of $[Cl^-]_i$ decreased from 54 (IQR 34) mM at P4–P5 to 40 (IQR 45) mM at P8–P10 and further down to 17 (IQR 22) mM in the P18–P51 group (Fig. 5*D*). These data are in agreement with measurements of the ion transport efficacy of KCC2 in cortical neurons in vitro, which show strong up-regulation commencing at around P6, with near-maximum extrusion rates achieved at ~P14–P16 (3, 36).

The high $[Cl^-]_i$ in immature neurons is generally thought to be maintained by Cl^- uptake via NKCC1 (in the Introduction). Consistent with data obtained in vitro, superfusion of the cortex of P4–P5 mice with saline containing the NKCC1 inhibitor bumetanide (55 μM) resulted in a pronounced decrease of median $[Cl^-]_i$ to 21 mM (IQR 22 mM; five mice, n = 381 neurons) (Fig. 6 *A* and *B*). Application of the vehicle only had no discernible effect on $[Cl^-]_i$ (53 mM; IQR 38 mM; four mice, n = 126 neurons).

Fig. 5*D* shows that the P8–P10 group has a large variability, which might be because of the presence of both immature and more mature neurons, leading to a mosaicism with regard to neurons with low and high $[Cl^-]_i$. The pups in this age group are large enough to enable implanting them with a perforated optical window that could be microperfused with bumetanide. In four mice at P8–P10 (n = 166 neurons), we imaged the same neurons before and after bumetanide to establish whether a high initial value of $[Cl^-]_i$ (reflecting cellular immaturity) would be predictive of a larger effect of the NKCC1 blocker. Fig. 6 *C*–*E* shows that the treatment caused a shift of $[Cl^-]_i$ toward lower values in each individual neuron and that, indeed, the amplitude of the shift correlated with the initial chloride level.

Dynamic Imaging of H^+ and Cl^- Ions in Vivo. During network activity, $[Cl^-]_i$ and pH_i are modulated by channel-mediated fluxes driven by ionic driving forces for Cl^- and for channel-permeant acid–base
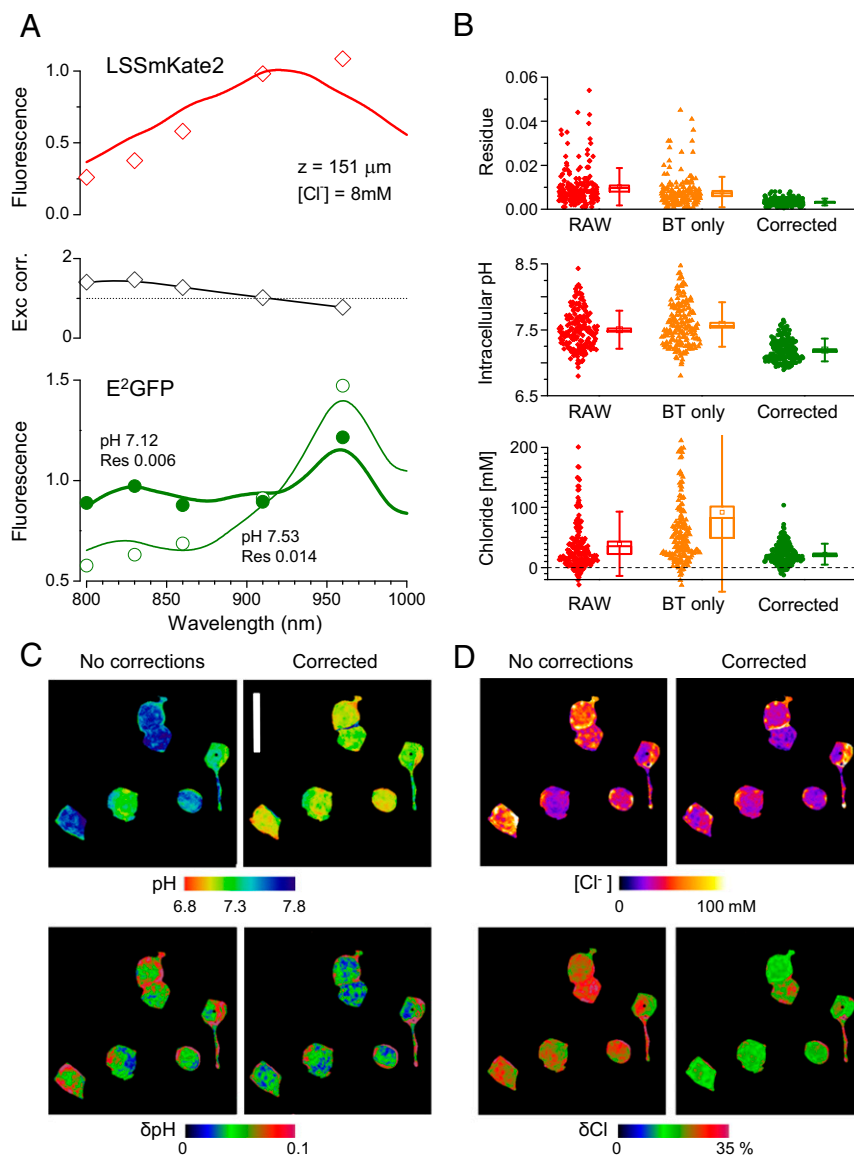
**Fig. 4.** Computation of pH_i and $[Cl^-]_i$. (*A*) Open symbols show the excitation spectrum of LSSmKate2 measured at the depth of 150 µm in a P18 mouse. The red line in *Top* is the LSSmKate2 spectrum obtained in the absence of excitation scattering. As expected, there is more loss of fluorescence at shorter excitation wavelengths. *Middle* depicts the ratio between the reference and the observed spectra. This correction was applied to the E^2GFP spectrum as shown in *Lower*: the open symbols are the original data (after bleed-through correction), and the filled symbols have been corrected for excitation scattering. The lines show the results of the linear decomposition before (thin line) and after (thick line) correction. The resulting pH and fit residuals (Res) are also reported. It is obvious that the distortion of the excitation spectrum causes an artifactual shift to higher pH values. (*B*, *Top*) Each symbol represents the residue of the fit of each neuron computed from raw data (red), with correction for bleed through only (BT; orange), and fully corrected for excitation and emission scattering (green). The corrections improve the fit of the spectra, thus decreasing the residues. Furthermore, the dispersion of the computed pH_i and $[Cl^-]_i$ (*B*, *Middle* and *Bottom*) is decreased. Box charts show averages, medians, SEs, and SDs. (*C* and *D*) The pH_i and $[Cl^-]_i$ maps, computed before and after correction for excitation scattering and emission extinction, show the decrease of data variability, which is also mirrored by the decrement of the uncertainties δpH and δCl computed on each pixel (pseudocolor maps in *Lower*) (*Supporting Information*). Images have been obtained at a depth of 200 µm in a P32 mouse. (Vertical scale bar: 25 µm.)

species (mainly HCO_3^-), respectively. However, active transport of Cl^- and H^+/HCO_3^- will oppose the effects of the passive fluxes, and thus, the instantaneous ion concentrations are set by the properties of the ion channel/transporter relationships (3).

So far, there are no data on intracellular Cl^- and pH dynamics in cortical neurons in vivo. Measurements of the steady-state values of pH_i and $[Cl^-]_i$ based on sampling the excitation spectra at several wavelengths are inherently slow and cannot provide time-resolved data. However, Eq. 7 (*Materials and Methods*) shows that it is possible to measure simultaneously pH_i and $[Cl^-]_i$ by alternating only two different excitation wavelengths. In these experiments, excitation was provided by two tunable lasers, which were steered and combined before the scanning head, and alternatively selected by electromechanical shutters during acquisition (Fig. 7 *A* and *B*). We constructed time-lapse sequences by alternating excitation at 860 nm and at the isosbestic point at 910 nm: each pair of E^2GFP images provides an estimate of pH_i, while the LSSmKate2 images provide the signal for the correction of excitation power at the focal plane and the reference for computation of $[Cl^-]_i$.

We performed dynamic measurements of pH_i and $[Cl^-]_i$ in vivo after induction of hypercapnia by inhalation of a gas mixture containing 30% CO_2 in air. Breathing this gas mixture induces

fast acidification of the brain extracellular space and brain tissue (37), leading to suppression of neuronal activity involving multiple mechanisms, such as enhancing GABAergic transmission (1), as well as inhibition of NMDA receptors and voltage-gated Na^+ and Ca^{2+} channels (38, 39). Time-lapse imaging was performed while recording the LFP with an intracortical electrode inserted in the optic window. Fig. 7*C* shows that, at the beginning of the recording (t < 60 s), the LFP is dominated by slow oscillations in the δ-band (0.5–4 Hz) characteristics of slow-wave sleep and present under urethane anesthesia. Acidification begun within 20 s from the onset of CO_2 inhalation and network activity rapidly subsided (Fig. 7 *C* and *D*). The excitation spectra of LSSmClopHensor rapidly shifted toward the acidic form, reaching a plateau level within a few minutes from hypercapnia onset (Fig. 7 *E* and *F*). In four mice (>P35), we observed a similar behavior and kinetics, with an average fall in pH_i of 0.6 ± 0.3. The intraneuronal acidosis was paralleled by a fast drop in $[Cl^-]_i$, which is probably caused by the cessation of neuronal activity and/or by the actions of plasmalemmal chloride/bicarbonate transporters in response to the fall in pH_i (1). An alkaline shift was observed immediately at the end of the CO_2
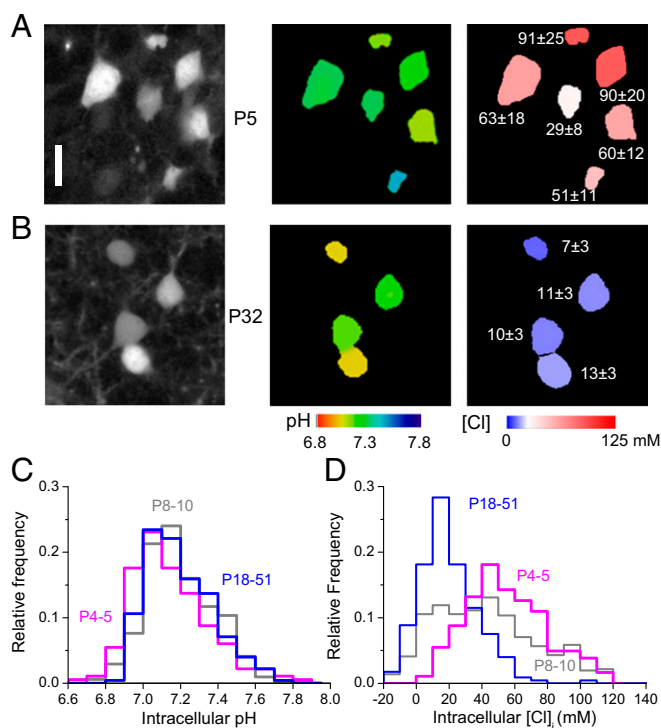
Fig. 5. Developmental shift of steady-state intraneuronal chloride concentration in vivo. (*A* and *B*) Two-photon imaging in a P5 mouse (*A*) and in a P32 mouse (*B*). The color images show pH$_i$ and [Cl$^-$]$_i$ maps for each cell in the field. The numbers in *Right* indicate [Cl$^-$]$_i$ of the adjacent neuron and the computed error. (Vertical scale bar: 15 μm.) (*C* and *D*) Distributions of values of [Cl$^-$]$_i$ and pH$_i$ in three different age groups as shown. Note the robust developmental shift of [Cl$^-$]$_i$ to lower levels shown here in vivo. Data pooled from nine mice at P4–P5, eight at P8–P10, and five at the age of P18–P51. The distribution of [Cl$^-$]$_i$ is strikingly different in the three age groups (Kolmogorov–Smirnov test, $P < 0.001$), while the respective pH$_i$ levels are closely overlapping.

inhalation together with the gradual reappearance of network activity (Fig. 7 *C–E*).

To trigger a robust, seizure-like network event, we applied the potassium channel blocker 4-aminopyridine (4-AP) on the occipital cortex of adult mice (40) under light urethane anesthesia. In these experiments, the cranial window was sealed with a perforated coverslip to apply a droplet of 100 mM solution of 4-AP in saline. As observed previously in superfused slices and after in vivo i.p. injection (40, 41), epileptiform activity started within 30 min from drug application. Fig. 8*A* shows the LFP recorded during a cortical seizure, which was characterized by a large increase of oscillatory activity in a wide bandwidth (Fig. 8*B*). Dynamic imaging of [Cl$^-$]$_i$ showed a rapid net accumulation of Cl$^-$ (Fig. 8*C*) in parallel with the temporal evolution of fast oscillations in the γ band (Fig. 8*D*). These data indicate that active Cl$^-$ extrusion was overwhelmed by the channel-mediated load that is most likely attributable to GABA$_A$R-mediated Cl$^-$ influx triggered by the intense interneuronal activity present in this model (42). Similar results were obtained in five mice (>P35), where [Cl$^-$]$_i$ was elevated by 22 ± 7 mM. In all cases, the recovery of [Cl$^-$]$_i$ commenced immediately after the abrupt end of seizure activity. Interestingly, there was also a fall in pH$_i$ that had a slower time course than the increase in [Cl$^-$]$_i$. These data do not permit identification of the underlying mechanism, but both a GABA$_A$R-mediated efflux of HCO$_3^-$ and a production of metabolic acid are likely to contribute to the cellular acidosis, which in fact, is characteristic of seizures and seizure-like activity (26, 43).

Discussion

Properties and Advantages of LSSmClopHensor in Neuronal Ion Imaging.
In this study, we have developed a method for simultaneous two-photon in vivo imaging of [Cl$^-$]$_i$ and pH$_i$ in individual cortical pyramidal neurons based on LSSmClopHensor, a genetic ion indicator consisting of an ion-sensitive GFP (E^{2}GFP) and an ion-insensitive red fluorescent protein (LSSmKate2) that provides a ratiometric reference. One of our main findings is that in vivo ion imaging in general, even if done in a ratiometric manner, is strongly affected by the wavelength-dependent extinction of light as it propagates through brain tissue. This effect, whereby shorter wavelengths are absorbed more efficiently as a function of imaging depth, leads to a significant distortion of excitation spectra and to a red shift of fluorescence. Since the optical properties of LSSmKate2 are independent of Cl$^-$ and pH, we have been able to use its signal to correct for the above source of error. Notably, the approach used in this correction was verified in FLIM measurements of pH$_i$, which are insensitive to light absorption within brain tissue. To show the utility of our methodology, we provide here direct in vivo evidence for the developmental shift to lower intraneuronal [Cl$^-$] levels that takes place during neuronal maturation and for the specific role of bumetanide-sensitive Cl$^-$ accumulation in neonatal neurons, which is required for their widely studied depolarizing GABA$_A$R responses. We also introduce a method for dynamic monitoring of changes in pH$_i$ and [Cl$^-$] in vivo, exemplified here as responses to hypercapnia and seizure activity.

Several ion sensors based on GFP have been developed (20), starting from Clomeleon (44). Clomeleon consists of the fusion of CFP and Topaz, a YFP mutant, with fluorescence that is reduced on binding with Cl$^-$ ions. When exciting CFP and recording emission from CFP and FRET emission from Topaz, an increase in Cl$^-$ causes a reduction of the Topaz fluorescence. Clomeleon signal has a complex pH dependence, and its apparent K_d spans two orders of magnitude in the pH range from 6 to 8. At physiological pH, the reported K_d for Cl$^-$ (about 160 mM) is far from physiologically meaningful [Cl$^-$]$_i$ levels (44–46). The above properties as well as the distortion present in deep tissue imaging imply that Clomeleon offers little sensitivity and reliability at the low concentrations expected in adult neurons.

Wimmer et al. (47) provided fluorometric data on [Cl$^-$]$_i$ changes in vivo by using SuperClomeleon (48), which has a somewhat higher affinity (20–40 mM) to Cl$^-$ than Clomeleon. This study has important differences from our approach, since they could only measure bulk changes of [Cl$^-$]$_i$ concentration in a relatively large brain volume. This is also true for a more recent study by Berglund et al. (49) on tonic GABAergic inhibition in the cerebellum, where the authors performed [Cl$^-$]$_i$ imaging at cellular level in slices and used bulk measurements in vivo. Finally, it is obvious that, in experiments with SuperClomeleon, it is not possible to make a correction for pH$_i$ differences and dynamic changes at the level of individual neurons even in vitro, which would be required for a valid estimate of [Cl$^-$]$_i$ based on the highly pH-sensitive Cl$^-$ signal of this indicator. Here, it is noteworthy that neuronal pH$_i$ shows relatively large cell-to-cell variations (Fig. 5), even under steady-state conditions (50).

The Developmental Shift in Neuronal [Cl$^-$]$_i$.
Despite the extensive electrophysiological data obtained in vitro, which are supported by a wide range of molecular biological studies on the expression patterns and properties of NKCC1 and KCC2 (3, 4), the presence of the ontogenetic decrease in [Cl$^-$]$_I$, and the consequent shift in E$_{GABA}$, have been and are still being debated (12). A key element in this debate is the absence so far of direct in vivo demonstration of the Cl$^-$ shift. In this study we provide direct evidence for this developmental phenomenon. Our imaging data, based on a total of ~900 individual pyramidal neurons in three age groups, show a

Fig. 6. A high intracellular chloride concentration is maintained by the NKCC1 cotransporter in immature neurons. (*A*) Effect of local application of the NKCC1 inhibitor bumetanide on $[Cl^-]_i$. This treatment caused a drastic reduction of intracellular chloride, indicating that the high $[Cl^-]_i$ in newborn mice is maintained by the operation of NKCC1. White in the horizontal pseudocolor calibration bar corresponds to $[Cl^-]_i = 25$ mM. The numbers in *Right* indicate $[Cl^-]_i$ of the adjacent neuron and the computed error. (Vertical scale bar: 25 μm.) (*B*) Superimposed distributions of $[Cl^-]_i$ at P4–P5 under control conditions (area under red curve; vehicle, four mice) and after treatment with bumetanide (area under green curve; seven mice, Kolmogorov–Smirnov test, $P < 0.001$). (*C*) Paired imaging before and 40 min after superfusion with bumetanide in a P10 mouse. The same cells were imaged before and after the administration of bumetanide through a tiny perforation of the imaging chamber. All cells in the field displayed a decrease in $[Cl^-]_i$. (Vertical scale bar: 25 μm.) (*D*) Scatterplot showing the concentration of all cells recorded before and after bumetanide (Bume) treatment. Different symbols refer to four different mice. The majority of cells fall under the line, which has a slope of one, indicating that the treatment caused a decrement of $[Cl^-]_i$. (*E*) The size of the drop of $[Cl^-]_i$ correlates positively with the initial concentration. Adjusted $R^2 = 0.49$.
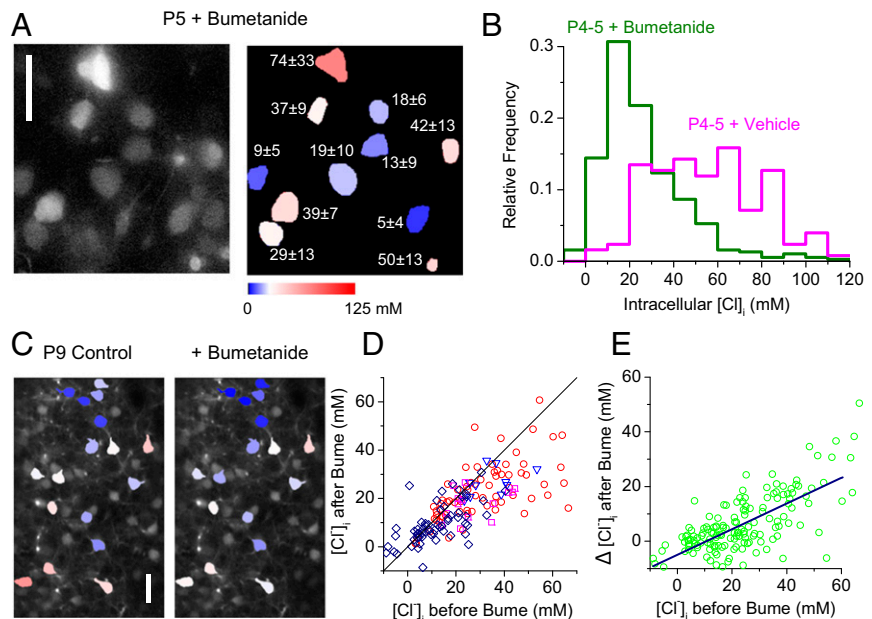

robust fall in somatic $[Cl^-]_i$ from P4–P5 to P8–P10, with a further decrease to mature levels at P18–P51. The validity of our data is further corroborated by the large decrease in $[Cl^-]_i$ caused by bumetanide, a potent blocker of the Cl^- uptake transporter NKCC1. The effect of bumetanide was clearly seen both at the population level and in individual neurons. Regarding the latter, bumetanide had a more pronounced effect on $[Cl^-]_i$ in individual neonatal neurons with a high steady-state chloride level, which indicates a higher basal activity of NKCC1. These data are in agreement with a recent in vivo study on intraneuronal Ca^{2+} imaging, which reports the presence of bumetanide-sensitive depolarizing actions of GABA in occipital cortical neurons in P3–P4 mice (9).

The median estimate of the mature somatic $[Cl^-]_i$ corresponds to an E_{Cl} of -55 mV in the P18–P51 age group, which is somewhat more positive than one would expect on the basis of currently available electrophysiological data on E_{GABA} (3). Here, we would like to note that the electrophysiological measurements have been typically done in quiescent tissue in vitro (i.e., in the absence of a significant activity-dependent Cl^- load that must be present even under physiologically normal in vivo conditions). Another factor worth recalling is that, because of neuronal pH_i regulation, the intracellular concentration of bicarbonate leads to an inwardly directed driving force for the HCO_3^--mediated current across $GABA_A$Rs. However, under these conditions, assuming a relative HCO_3^-/Cl^- permeability of 0.2–0.3, there is a very modest bicarbonate-dependent effect of about $+3–5$ mV on the reversal potential (1), yielding a median E_{GABA} value around $\sim-51–53$ mV. Given the substantial scatter in the primary data on $[Cl^-]_i$ and the steep dependence of E_{GABA} on $[Cl^-]_i$, we do not maintain that our estimates of E_{GABA} are in ideal agreement with quantitative electrophysiological considerations; a perfect match at this pioneering stage of in vivo Cl^- imaging would be unexpected.

Intraneuronal Steady-State pH and the Effect of Hypercapnia. Our two-photon imaging data show that pH_i in pyramidal neurons is around 7.16 in P18–P51 neurons, with no changes during postnatal development. As stated above, using FLIM in P18–P51 neurons gave values that were practically identical with those obtained by spectroscopic imaging. As a whole, the pH_i data obtained under physiological conditions are in good agreement with those published before in in vitro work (22, 23). Exposure to hypercarbic conditions (CO_2 elevated to 30%) brought about a block in neuronal activity associated with an acidosis with an amplitude that is consistent with analogous experiments in vitro (24).

Seizure-Induced Changes in Neuronal $[Cl^-]_i$ and pH_i. Unlike in the quasisteady-state conditions, which often prevail in experiments in vitro, neurons in vivo are never silent, and therefore, local intraneuronal ion concentrations are modulated in an activity-dependent manner, primarily imposed by changes in driving force. While both synaptic and extrasynaptic $GABA_A$Rs as well as nonsynaptic GlyRs provide the major conductive pathways, there are additional Cl^- channels, such as ClC-2, that may also contribute to the activity-induced changes in $[Cl^-]_i$ (4). Indeed, activity-dependent elevations of $[Cl^-]_i$, can be of sufficient magnitude to transiently reverse the polarity of IPSPs in mature neurons from hyperpolarizing to depolarizing and even to become functionally excitatory (3, 24). This kind of manifestation of ionic plasticity at synapses must have a profound effect on the properties of neuronal networks, and therefore, dynamic monitoring of Cl^- at the cellular level in vivo is of much interest. Moreover, intense neuronal activity is known to lead to a fall in pH_i that is attributable to the generation of metabolic acid, such as lactate, as well as $GABA_A$R-mediated net efflux of HCO_3. The activity-dependent neuronal acidosis is considered to present one of those intrinsic mechanisms, which suppress an overt increase in network excitability, such as seizures (24). In light of the above considerations, we used a double-ratiometric method to simultaneously image $[Cl^-]_i$ and pH_i at the level of single pyramidal neurons during seizure-like activity induced by the K^+ channel blocker 4-AP (40), and our data show that it is possible to monitor both ion concentrations at a frame rate which is sufficiently high to yield physiologically relevant data, qualitatively similar to what has been shown in work on brain slices (21, 51, 52). Our data show that cortical seizures are accompanied by an increase in $[Cl^-]_i$, tightly limited to the window of intense network activity. Moreover, we observed a delayed and slow fall in pH_i, which is in agreement with analogous data obtained in dynamic measurements of brain tissue pH in vitro (26, 43).
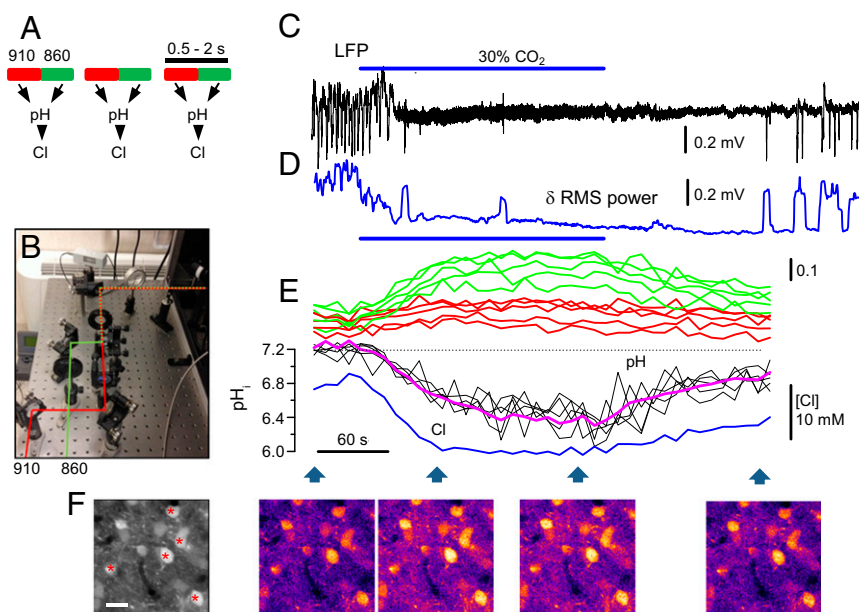
Fig. 7. Dynamic imaging of pH$_i$ and Cl$_i$ in vivo during hypercapnia induced by CO$_2$ inhalation. (*A*) Schematics of the acquisition processes: the sensor is excited alternatively at 910 and 860 nm by using two tunable lasers controlled by fast electrometrical shutters. The two fluorescence images can be obtained within 500 ms, and successive pairs can be acquired at the desired interval. The alternated images are used to compute pH. The chloride estimate is then obtained by the green to red emission ratio. (*B*) Schematic of the excitation pathway. The beams emerge from the shutters (not depicted) with orthogonal polarization, and they are combined with a polarizing beam splitter before entering in the scanning head. (*C*) LFP recorded in the occipital cortex of a P35 mouse anesthetized with urethane (band pass 0–4 Hz). The initial phase of the recording shows the characteristic oscillations present during slow-wave sleep characterized by a strong enhancement of the δ band of the EEG. The hypercarbic condition was induced by letting the mouse breath a mixture of 30% CO$_2$ in air with a face mask (blue horizontal line). (*D*) The rms power of the δ band EEG signal drops rapidly after the onset of hypercarbia. (*E*) Time course of E^{2}GFP fluorescence after correction for bleed through and excitation loss. Red and green traces indicate the time course of fluorescence excited at 860 and 910 nm (green and red, respectively). Hypercarbia causes a clear increase of the fluorescence of the protonated peak, indicating intracellular acidification. The ratio of the two channels provides the pH measurement as shown in the traces for five different cells in the field (thin black lines) and for the neuropile (thick red line) in *Lower*. At this time resolution, all cells and the neuropile show a remarkably similar behavior. A representative trace from one cell in the field shows a decrement of [Cl$^-$]$_i$ (thick blue line) as pH$_i$ falls and the network activity becomes suppressed. (*F*) Sample images of the fluorescence excited at 860 nm at the time points indicated by the arrowheads. The leftmost panel represents a maximum projection of the entire stack, and the five cells reported in the fluorescence recordings are identified by red stars. (Scale bar: 20 μm.)

It is worth noting that the time constant of Cl$^-$ interaction with LSSmClopHensor is identical to that of ClopHensor (29) and similar to that of Clomeleon and SuperClomeleon (53). This implies that the sensor signal is not likely to fully reflect the fast changes in [Cl$^-$]$_i$ that are bound to take place during seizures, but as is the case with genetically encoded sensors for calcium- and ion-sensitive K$^+$ microelectrodes, ionic dynamics measured at rates corresponding to the present do provide useful information on the direction, magnitude, and time course of the net activity-induced Cl$^-$ flux.

Conclusions

This study introduces a technique for simultaneous two-photon in vivo imaging of intraneuronal [Cl$^-$] and pH based on LSSmClopHensor. This genetic sensor is constructed by fusion of an ion-sensitive GFP (E^{2}GFP) with a red fluorescent protein (LSSmKate2), which provides a ratiometric reference. Since the optical properties of LSSmKate2 are insensitive to Cl$^-$ and pH, we have been able to use its signal to correct for effects attributable to the optical properties of brain tissue. This methodology opens up several avenues for exploring the development and functional properties of neuronal ion regulation, as well as identifying mechanisms involved in the etiology and endophenotypes of a wide variety of brain disorders. The regulatory mechanisms of [Cl$^-$]$_i$ are involved in a wide range of acute neuronal insults, such as ischemia or traumatic injury, as well as in chronic disorders, including epilepsy, autism, and Down syndrome. Regulation of [Cl$^-$]$_i$ is also a major player in the control of neuroendocrine responses (54–56), and a very recent study

puts KCC2 in key position in synaptic plasticity mechanisms that are likely to underlie cognitive impairment during senescence (57). These wide-ranging observations extend the scope and impact of technical advances in in vivo Cl$^-$ imaging.

Materials and Methods

Animals and Procedures for in Vivo Imaging. LSSmClopHensor was transduced by in utero electroporation in CD-1 mice at embryonic day 15.5 to transfect neuronal progenitors of layer 2/3 pyramidal neurons of the visual cortex (30). Before imaging, mice were anesthetized with an i.p. injection of urethane (1–1.5 g/kg). Craniotomy (2- to 3-mm diameter) was performed as described elsewhere, and the dura mater was removed to reduce light scattering (58). A custom-made steel head post with a central imaging chamber was glued to the skull. Hypercarbia was induced by exposing the animals to a mixture containing 30% CO$_2$ in ambient air. This study was performed in strict accordance with the recommendations of the Italian Ministry of Health (Dlg. 26/14) and according to protocol 277/2015-R approved by the Ministry of Health on April 23, 2015.

Solutions. The composition of the sterile saline solution was 126 mM NaCl, 3 mM KCl, 1.2 mM KH$_2$PO$_4$, 1.3 mM MgSO$_4$, 26 mM NaHCO$_3$, 2.4 mM CaCl$_2$, 15 mM glucose, and 10 mM Hepes, pH 7.4. A 4-μL aliquot of bumetanide stock solution (50 mg/mL in DMSO) was sonicated in 10 mL of saline, and a bolus of a few microliters was applied on the cortex before sealing of the imaging chamber.

Bleed-Through Correction for LSSmClopHensor. Fig. S1*A* shows the two-photon excitation spectra of purified LSSmClopHensor obtained by providing the same number of photons at each wavelength. As expected, the spectra measured in the green channel strongly depend on pH. The pH dependency was also observed in the red channel as a result of bleed through of the E^{2}GFP emission. The magnitude of bleed through was determined by purifying separately the proteins composing the sensor (E^{2}GFP and LSSmKate2) (details are in *Supporting Information*) and by measuring their fluorescence in both emission
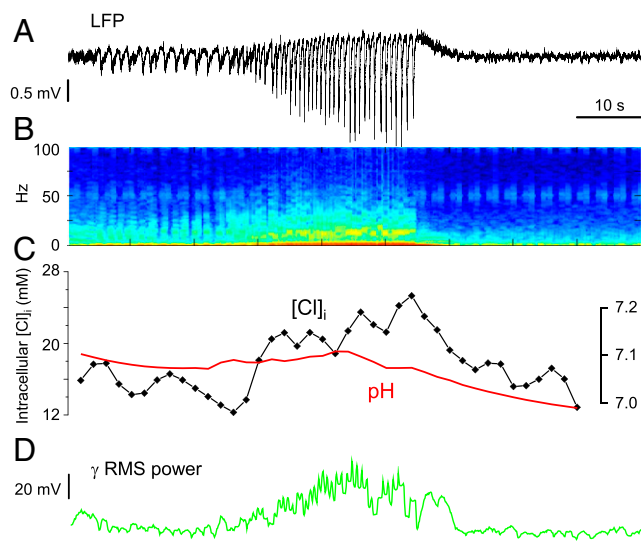
Fig. 8. Dynamic imaging of pH_i and Cl_i during epileptic seizure in vivo. (*A*) Seizures were triggered in the occipital cortex in vivo in an adult mouse (about 2 mo of age) by means of localized treatment with the convulsive agent 4-AP. The trace shows the LFP recorded during a seizure characterized by high-frequency firing and a large increase of the power spectra at both low and high frequencies (*B*). (*C*) The simultaneous measurement of pH_i and Cl_i shows a sharp chloride increase at the onset of the seizure; note also the long-lasting intracellular acidification during and after seizure. (*D*) The temporal profile of the chloride influx correlates with the profile of the rms power in the γ band (30–80 Hz). The recovery of chloride begins immediately at the end of high-frequency firing.

channels (Fig. S1*B*). These data provided the coefficients $\alpha(\lambda)$ and $\beta(\lambda)$ that describe the cross-talk between the emission channels (Fig. S1*C*). The fluorescence of E^2GFP and LSSmKate2 corrected for bleed through is given by the following system of linear equations:

$$\begin{cases} G_*(\lambda) = G_{raw}(\lambda) - \alpha(\lambda)R_*(\lambda) \\ R_*(\lambda) = -\beta(\lambda)G_*(\lambda) + R_{raw}(\lambda) \end{cases}, \qquad [6]$$

where G_{raw} and R_{raw} label the fluorescence measured in the green and red channels (after background subtraction and flat correction), and G_* and R_* indicate the fluorescence that originates from E^2GFP and LSSmKate2, respectively. LSSmClopHensor is characterized by the absence of intramolecular FRET, since LSSmKate2 has a very large Stokes shift: its peak of absorption (460 nm) is much bluer than the emission peak of E^2GFP (530 nm) (additional details are in *Supporting Information*).

To compare the sensor spectra obtained at different pH values, we had to consider that different samples had slightly different protein concentrations. Since the optical properties of LSSmKate2 are not influenced by pH, we normalized each spectrum at the peak of R_*, and this normalization is used through the study.

Measurement of pH and Calibration of LSSmClopHensor. The excitation spectrum of LSSmClopHensor at a given pH, $G_{*pH}(\lambda)$, can be described as the linear combination of the protonated $(G_{*6.0})$ and deprotonated $(G_{*8.0})$ spectra according to the equation:

$$G_{*pH}(\lambda) = \delta G_{*6.0}(\lambda) + \varepsilon G_{*8.0}(\lambda). \qquad [7]$$

This is a set of n equations, where n is the number of wavelengths at which spectra are sampled. If n = 2, the system can be solved analytically according to the standard ratiometric analysis. A larger set of excitation wavelengths provides a result that is less sensitive to errors, and δ and ε can be determined by minimizing the sum of the residues R defined as

$$R = \sum_{i=1}^{n} \left(G_{*pH}(\lambda_i) - \left(\delta G_{*6.0}(\lambda_i) + \varepsilon G_{*8.0}(\lambda_i) \right) \right)^2. \qquad [8]$$

The size of the residue is an indicator of the quality of the fit. We applied this procedure to the dataset of Fig. 1*B*: for each spectrum, we determined δ and ε

(details are in *Supporting Information*). Fig. 1*C* shows the decomposition of the E^2GFP spectrum. A calibration curve can be obtained by the relationship between the polar angle $\theta = \text{atan}(\varepsilon/\delta)$ (Fig. 1*D*) and the pH of the fitted spectra. The calibration is fitted with the following sigmoidal function:

$$\theta = \theta_L + \frac{\theta_R - \theta_L}{1 + 10^{(pK_a - pH)a}}, \qquad [9]$$

where pK_a is the affinity for H^+. Table S1 shows the values of the fit parameters (θ_R, θ_L, pK_a, and a) at three different temperatures (24 °C, 31 °C, and 36 °C). The corresponding functions are reported in Fig. S2*B*. The calibrations were repeated periodically, and they showed only minimal changes.

Computation of the Intracellular Chloride Concentration. Because Cl^- binds solely to the protonated form of E^2GFP, only a fraction of the sensor fluorescence depends on $[Cl^-]_i$, and this fraction in turn depends on pH. This is summarized by the following equation (59):

$$K_d^{Cl}(pH) = 13.1 \frac{1 + 10^{(pK_a - pH)}}{10^{(pK_a - pH)}}, \qquad [10]$$

where 13.1 mM is the Cl^- affinity for fully protonated E^2GFP (29), and the term on the right is the inverse of the fraction of nonprotonated sensor (i.e., the fraction that is Cl^--insensitive). Finally, $[Cl^-]_i$ is given by

$$[Cl] = K_d^{Cl}(pH) \left(\frac{r(0)}{r(Cl)} - 1 \right), \qquad [11]$$

where r(0) is the ratio between the fluorescence of E^2GFP and LSSmKate2 measured at the isosbestic point when $[Cl^-]_i = 0$ (Table S1). The term r(Cl) is the same ratio measured at a given $[Cl^-]_i$.

Calibration of LSSmClopHensor: Measurements in Solution and in HEK293T Cell Cultures. The protein calibration set provides correct results only if the sensor behaves identically in solution and in the cytoplasm or if one can correct for the difference between solution and cellular environment. Since the optical properties of the chromophore are affected by the surrounding cellular environment (60), we repeated the pH calibration in HEK293T cells in the presence of ionophores that dissipate the transmembrane pH gradient. After scoring the pH of each dataset with the median of the distribution (Fig. S7*A*), we observed that the spectroscopic estimate of pH was systematically more acidic than the pH of the extracellular calibration media. From these data (Fig. S7*B*), we obtained an empirical equation that allows us to correct the pH_i computed by the spectroscopy data for the effects caused by the intracellular environment:

$$pH_{Cor} = -162.70 + 72.83\, pH_{Sp} - 10.57\, pH_{Sp}^2 + 0.52\, pH_{Sp}^3. \qquad [12]$$

HEK293T cells were incubated with the calibration buffer (20 mM Hepes, 0.6 mM $MgSO_4$, 38 mM sodium gluconate, 100 mM potassium gluconate) supplemented with ionophores mixture to equilibrate extra- and intracellular ion concentrations (5 μM K^+/H^+ exchanger nigericin, 5 μM protonophore carbonyl cyanide p-chlorophenylhydrazone, 5 μM K^+ ionophore valinomycin, 10 μM Cl^-/OH^- exchanger tributyltin chloride). Cells were treated with a succession of five washes to allow equilibration of pH.

In Vivo Two-Photon Imaging. In vivo two-photon imaging was performed on a Prairie Ultima Multiphoton microscope equipped with two mode-locked Ti: Sapphire lasers (Coherent Chameleon Ultra II and Coherent Verdi-Mira). For each field, a set of images was acquired at different excitation wavelengths (ranging in number from 5 to 11). Acquisitions were performed with a water immersion lens (60×, 1.00 N.A.; Olympus) at a resolution of 512 × 512 pixels and at zoom 2, leading to a field of 102 × 102 μm and a linear resolution of 0.2 μm per pixel. Before each imaging session, we measured the power of the excitation laser at the optic bench and at the output of the objective lens for each wavelength used. This conversion function is required to infer the power at the sample (which is not accessible after the mouse is placed under the objective) from the power measured on the optic bench.

Time-lapse imaging was performed by alternating the excitation from the two lasers tuned at 860 and 910 nm. The two beams have been adjusted to have orthogonal polarization, so that they can be combined by a polarizing beam splitter. Two different sets of mirrors placed before the beam splitter were used for coalignment. The wavelength was selected by fast electromechanical shutters synchronized to the microscope scanning unit. The data were analyzed by custom ImageJ macros.

Criteria for Data Rejection and Statistical Procedures. For each cell, we computed the error on the final chloride estimate by propagating the residue of the fit (Eq. **8**) following the computation described by Eqs. **S1–S20**. Since a reliable pH_i estimate is necessary for a proper final determination of $[Cl^-]_i$, the average error for pH was determined, and cells that presented an error larger than twice the mean error were excluded from following analysis. When $[Cl_i]$ is in the few millimolar range, the ratio $r(Cl)$ of the E^2GFP and LSSmKate2 fluorescence is close to $r(0)$, and therefore, because of experimental error on the fluorescence estimate, Eq. **11** can occasionally yield negative values for the Cl^- measurements. This is an unavoidable consequence of the propagation of experimental errors, and we decided not to exclude these data from the population. Statistics were computed with Origin 8. Nonparametric distributions were compared with the paired Wilcoxon rank test or with the Kolmogorov–Smirnov test as indicated in the figures.

1. Kaila K (1994) Ionic basis of GABAA receptor channel function in the nervous system. *Prog Neurobiol* 42:489–537.
2. Raimondo JV, Markram H, Akerman CJ (2012) Short-term ionic plasticity at GABAergic synapses. *Front Synaptic Neurosci* 4:5.
3. Kaila K, Price TJ, Payne JA, Puskarjov M, Voipio J (2014) Cation-chloride cotransporters in neuronal development, plasticity and disease. *Nat Rev Neurosci* 15:637–654.
4. Doyon N, Vinay L, Prescott SA, De Koninck Y (2016) Chloride regulation: A dynamic equilibrium crucial for synaptic inhibition. *Neuron* 89:1157–1172.
5. Kahle KT, et al. (2013) Modulation of neuronal activity by phosphorylation of the K-Cl cotransporter KCC2. *Trends Neurosci* 36:726–737.
6. Kaila K, Ruusuvuori E, Seja P, Voipio J, Puskarjov M (2014) GABA actions and ionic plasticity in epilepsy. *Curr Opin Neurobiol* 26:34–41.
7. Luhmann HJ, et al. (2016) Spontaneous neuronal activity in developing neocortical networks: From single cells to large-scale interactions. *Front Neural Circuits* 10:40.
8. Kriegstein AR, Owens DF (2001) GABA may act as a self-limiting trophic factor at developing synapses. *Sci STKE* 2001:pe1.
9. Kirmse K, et al. (2015) GABA depolarizes immature neurons and inhibits network activity in the neonatal neocortex in vivo. *Nat Commun* 6:7750.
10. Rivera C, et al. (1999) The K+/Cl- co-transporter KCC2 renders GABA hyperpolarizing during neuronal maturation. *Nature* 397:251–255.
11. Coombs JS, Eccles JC, Fatt P (1955) The specific ionic conductances and the ionic movements across the motoneuronal membrane that produce the inhibitory post-synaptic potential. *J Physiol* 130:326–374.
12. Ben-Ari Y, et al. (2012) Refuting the challenges of the developmental shift of polarity of GABA actions: GABA more exciting than ever! *Front Cell Neurosci* 6:35.
13. Deidda G, Bozarth IF, Cancedda L (2014) Modulation of GABAergic transmission in development and neurodevelopmental disorders: Investigating physiology and pathology to gain therapeutic perspectives. *Front Cell Neurosci* 8:119.
14. Deidda G, et al. (2015) Reversing excitatory GABAAR signaling restores synaptic plasticity and memory in a mouse model of Down syndrome. *Nat Med* 21:318–326.
15. Cellot G, Cherubini E (2014) GABAergic signaling as therapeutic target for autism spectrum disorders. *Front Pediatr* 2:70.
16. Banerjee A, et al. (2016) Jointly reduced inhibition and excitation underlies circuit-wide changes in cortical processing in Rett syndrome. *Proc Natl Acad Sci USA* 113:E7287–E7296.
17. Cohen I, Navarro V, Clemenceau S, Baulac M, Miles R (2002) On the origin of interictal activity in human temporal lobe epilepsy in vitro. *Science* 298:1418–1421.
18. Begum G, et al. (2015) Inhibition of WNK3 kinase signaling reduces brain damage and accelerates neurological recovery after stroke. *Stroke* 46:1956–1965.
19. Löscher W, Puskarjov M, Kaila K (2013) Cation-chloride cotransporters NKCC1 and KCC2 as potential targets for novel antiepileptic and antiepileptogenic treatments. *Neuropharmacology* 69:62–74.
20. Arosio D, Ratto GM (2014) Twenty years of fluorescence imaging of intracellular chloride. *Front Cell Neurosci* 8:258.
21. Paredes JM, et al. (2016) Synchronous bioimaging of intracellular pH and chloride based on LSS fluorescent protein. *ACS Chem Biol* 11:1652–1660.
22. Chesler M (2003) Regulation and modulation of pH in the brain. *Physiol Rev* 83:1183–1221.
23. Ruffin VA, Salameh AI, Boron WF, Parker MD (2014) Intracellular pH regulation by acid-base transporters in mammalian neurons. *Front Physiol* 5:43.
24. Ruusuvuori E, Kaila K (2014) Carbonic anhydrases and brain pH in the control of neuronal excitability. *Subcell Biochem* 75:271–290.
25. Raimondo JV, Irkle A, Wefelmeyer W, Newey SE, Akerman CJ (2012) Genetically encoded proton sensors reveal activity-dependent pH changes in neurons. *Front Mol Neurosci* 5:68.
26. Pavlov I, Kaila K, Kullmann DM, Miles R (2013) Cortical inhibition, pH and cell excitability in epilepsy: What are optimal targets for antiepileptic interventions? *J Physiol* 591:765–774.
27. Bizzarri R, et al. (2006) Development of a novel GFP-based ratiometric excitation and emission pH indicator for intracellular studies. *Biophys J* 90:3300–3314.
28. Piatkevich KD, et al. (2010) Monomeric red fluorescent proteins with a large Stokes shift. *Proc Natl Acad Sci USA* 107:5369–5374.
29. Arosio D, et al. (2010) Simultaneous intracellular chloride and pH measurements using a GFP-based sensor. *Nat Methods* 7:516–518.
30. Szczurkowska J, et al. (2016) Targeted in vivo genetic manipulation of the mouse or rat brain by in utero electroporation with a triple-electrode probe. *Nat Protoc* 11:399–412.
31. Gray NW, Weimer RM, Bureau I, Svoboda K (2006) Rapid redistribution of synaptic PSD-95 in the neocortex in vivo. *PLoS Biol* 4:e370.
32. Liu Z, Lavis LD, Betzig E (2015) Imaging live-cell dynamics and structure at the single-molecule level. *Mol Cell* 58:644–659.
33. Artoni P, Landi S, Sato SS, Luin S, Ratto GM (2016) Arduino Due based tool to facilitate in vivo two-photon excitation microscopy. *Biomed Opt Express* 7:1604–1613.
34. Brondi M, Sato SS, Rossi LF, Ferrara S, Ratto GM (2012) Finding a needle in a haystack: Identification of EGFP tagged neurons during calcium imaging by means of two-photon spectral separation. *Front Mol Neurosci* 5:96.
35. Feng G, et al. (2000) Imaging neuronal subsets in transgenic mice expressing multiple spectral variants of GFP. *Neuron* 28:41–51.
36. Khirug S, et al. (2005) Distinct properties of functional KCC2 expression in immature mouse hippocampal neurons in culture and in acute slices. *Eur J Neurosci* 21:899–904.
37. Albertazzi L, et al. (2011) Dendrimer-based fluorescent indicators: In vitro and in vivo applications. *PLoS One* 6:e28450.
38. Tombaugh GC, Somjen GG (1996) Effects of extracellular pH on voltage-gated Na+, K+ and Ca2+ currents in isolated rat CA1 neurons. *J Physiol* 493:719–732.
39. Traynelis SF, Cull-Candy SG (1990) Proton inhibition of N-methyl-D-aspartate receptors in cerebellar neurons. *Nature* 345:347–350.
40. Avoli M, et al. (1996) Synchronous GABA-mediated potentials and epileptiform discharges in the rat limbic system in vitro. *J Neurosci* 16:3912–3924.
41. Lévesque M, Salami P, Behr C, Avoli M (2013) Temporal lobe epileptiform activity following systemic administration of 4-aminopyridine in rats. *Epilepsia* 54:596–604.
42. Uva L, Breschi GL, Gnatkovsky V, Taverna S, de Curtis M (2015) Synchronous inhibitory potentials precede seizure-like events in acute models of focal limbic seizures. *J Neurosci* 35:3048–3055.
43. Xiong ZQ, Saggau P, Stringer JL (2000) Activity-dependent intracellular acidification correlates with the duration of seizure activity. *J Neurosci* 20:1290–1296.
44. Kuner T, Augustine GJ (2000) A genetically encoded ratiometric indicator for chloride: Capturing chloride transients in cultured hippocampal neurons. *Neuron* 27:447–459.
45. Berglund K, et al. (2006) Imaging synaptic inhibition in transgenic mice expressing the chloride indicator, Clomeleon. *Brain Cell Biol* 35:207–228.
46. Mukhtarov M, et al. (2013) Calibration and functional analysis of three genetically encoded Cl(-)/pH sensors. *Front Mol Neurosci* 6:9.
47. Wimmer RD, et al. (2015) Thalamic control of sensory selection in divided attention. *Nature* 526:705–709.
48. Grimley JS, et al. (2013) Visualization of synaptic inhibition with an optogenetic sensor developed by cell-free protein engineering automation. *J Neurosci* 33:16297–16309.
49. Berglund K, Wen L, Dunbar RL, Feng G, Augustine GJ (2016) Optogenetic visualization of presynaptic tonic inhibition of cerebellar parallel fibers. *J Neurosci* 36:5709–5723.
50. Bevensee MO, Cummins TR, Haddad GG, Boron WF, Boyarsky G (1996) pH regulation in single CA1 neurons acutely isolated from the hippocampi of immature and mature rats. *J Physiol* 494:315–328.
51. Lillis KP, Kramer MA, Mertz J, Staley KJ, White JA (2012) Pyramidal cells accumulate chloride at seizure onset. *Neurobiol Dis* 47:358–366.
52. Raimondo JV, et al. (2013) A genetically-encoded chloride and pH sensor for dissociating ion dynamics in the nervous system. *Front Cell Neurosci* 7:202.
53. Berglund K, Wen L, Augustine GJ (2015) Optogenetic sensors for monitoring intracellular chloride. *Optogenetics*, eds Yawo H, Kandori H, Koizumi A (Springer, Berlin), pp 159–183.
54. Kakizawa K, et al. (2016) A novel GABA-mediated corticotropin-releasing hormone secretory mechanism in the median eminence. *Sci Adv* 2:e1501723.
55. Maguire J (2014) Stress-induced plasticity of GABAergic inhibition. *Front Cell Neurosci* 8:157.
56. Hewitt SA, Wamsteeker JI, Kurz EU, Bains JS (2009) Altered chloride homeostasis removes synaptic inhibitory constraint of the stress axis. *Nat Neurosci* 12:438–443.
57. Ferando I, Faas GC, Mody I (2016) Diminished KCC2 confounds synapse specificity of LTP during senescence. *Nat Neurosci* 19:1197–1200.
58. de Vivo L, et al. (2013) Extracellular matrix inhibits structural and functional plasticity of dendritic spines in the adult visual cortex. *Nat Commun* 4:1484.
59. Arosio D, et al. (2007) Spectroscopic and structural study of proton and halide ion cooperative binding to gfp. *Biophys J* 93:232–244.
60. Kummer A, et al. (2002) Viscosity-dependent fluorescence decay of the GFP chromophore in solution due to fast internal conversion. *J Phys Chem B* 106:7554–7559.
61. dal Maschio M, et al. (2012) High-performance and site-directed in utero electroporation by a triple-electrode probe. *Nat Commun* 3:960.
62. Costa M, et al. (2006) Dynamic regulation of ERK2 nuclear translocation and mobility in living cells. *J Cell Sci* 119:4952–4963.
63. Cardarelli F, Serresi M, Bizzarri R, Giacca M, Beltram F (2007) In vivo study of HIV-1 Tat arginine-rich motif unveils its transport properties. *Mol Ther* 15:1313–1322.

Supporting Information

Sulis Sato et al. 10.1073/pnas.1702861114

Generation of the LSSmClopHensor Plasmid

LSSmClopHensor is based on the previously published ClopHensor (20), where the red signal was provided by the red fluorescent protein mDsRed. LSSmClopHensor was developed by joining E^{2}GFP with the Long Stokes Shift Monomeric protein LSSmKate2. LSSmClopHensor was cloned under the CAG promoter by the following procedure (21). A plasmid pCMV-MCS from the AAV Helper-Free System (catalog no. 240071; Agilent) was mutagenized with the oligos AscIFwdV2 5′-GGACCGATCCAGCCGGCGCGCCTTCGAATC-CCGGCC-3′ and AscIRevV2 5′-GGCCGGGATTCGAAGGCGCGCCGGCTGGATCGGTCC-3′ to introduce a restriction site for AscI. Subsequently, a fragment of CAG promoter was added to the mutagenized pCMV-MCS by digesting the Addgene plasmid 13777 with NcoI and NotI and by ligating the 1,361-bp fragment to the mutagenized pCMV-MCS digested with Nco alone to obtain pCAG-MCS. The correct orientation of the ligated fragment was evaluated by digesting the obtained plasmid with BamHI and EcoRI and with Xma alone. Then, E^{2}GFP-LSSmKate2 was amplified with PCR with the following primers: AscIGFPFwd 5′-GGCGCG-CCATGGTGAGCAAGGGCGAGGAGCT-3′ and XhoIClopHRev 5′-GCTAAACTCGAGGCCCTCTAGAGCACTAGCG-3′. The amplicon was digested with Asc and Xho and inserted into the pCAG-MCS plasmid that was previously digested with the same enzymes. The resulting pCAG-LSSmClopHensor plasmid was validated by sequencing. To amplify plasmid DNA, we used the Qiagen plasmid plus maxi kit (catalog no. 12965). Transformation of DNA was performed by using a recombinant free *Escherichia coli* strain (One Shot Stbl3 Chemically Competent *E. coli*; catalog no. C7373-03; Invitrogen).

Production of LSSmClopHensor Protein

The LSSmClopHensor plasmid, carrying an N-terminal His tag, was transformed in BL-21 *E. coli* expression strain (catalog no. C6010-03; Life Technology). Selected bacterial colonies were incubated at 37 °C in a Luria–Bertani growth medium with the addition of ampicillin. During the incubation, the OD_{600} was constantly monitored, and 1 mM IPTG (isopropyl β-D-1-thiogalactopyranoside) was added to the growth medium at $OD_{600} = 0.6$ to induce protein expression. The temperature of the incubator was lowered to 30 °C to decrease the bacteria replication rate and to increase protein expression. After 12 h, bacteria were centrifuged at $10,000 \times g$, and the supernatant was discarded. The pellet was suspended with the lysis buffer (100 mM Tris·HCl, 150 mM NaCl, 1 mM DTT, 0.05% Triton, pH 8). The mixture was then sonicated for five cycles of 30 s with an interval of 60 s; then, the lysate was centrifuged twice at $12,000 \times g$ for 1 h. The supernatant was incubated overnight with Ni-NTA agarose resin (catalog no. 30250; Qiagen). The resin was washed with the wash solution (100 mM Tris·HCl, 150 mM NaCl, 20 mM imidazole, pH 8). Finally, the stock solution of LSSmClopHensor was prepared by elution with washing buffer to reach a final protein concentration of about 100 μM (washing buffer composition: 100 mM Tris·HCl, 150 mM NaCl, 150 mM imidazole, pH 8).

Preparation of the LSSmClophensor Protein for Spectroscopy

Purified LSSmClophensor protein was washed by using 30-kDa Millipore cutoff filters to substitute the elution solution with H$_2$O. A stock solution for zero chloride pH calibration buffers was prepared as follows: 20 mM Hepes, 0.6 mM MgSO$_4$, 38 mM sodium gluconate, 100 mM potassium gluconate. From this base, vials of calibration solutions were prepared at several different pH values (6.0, 6.4, 6.8, 6.9, 7.0, 7.1, 7.2, 7.4, 7.6, and 8.0) at 24 °C. The pH of these calibration buffers was also measured at other temperatures of the calibration dataset (i.e., 31 °C and 36 °C).

Chloride calibration was performed as follows: the zero chloride buffer was mixed with a 138 mM chloride buffer (20 mM Hepes, 0.6 mM MgSO$_4$, 38 mM NaCl, 100 mM KCl) in different percentages to obtain chloride concentrations of 0.1, 5, 10, 30, 40, 70, and 138 mM. The pH of these mixtures was subsequently carefully adjusted by adding NaOH.

A 5-μL volume of unbuffered protein was added to 35 μL of each aliquot of calibration buffer to a final volume of 40 μL. The solution was placed in a spectroscopic chamber (catalog no. C-18139; Invitrogen) under the two-photon microscope using a thermostatic slide holder (Harvard Instruments).

pH Meter Calibration

pH meter (Seven Multi with a Hamilton BioTrode probe; Mettler Toledo) was calibrated at 24 °C, 31 °C, and 36 °C by using solutions of high-precision calibration buffers at pH 6.0, 7.0, and 8.0 (catalog nos. 33545, 242221, and 33547, respectively; Sigma-Aldrich). Calibration buffers were warmed at the proper temperature, and the pH was adjusted according to the temperature sensitivity of each buffer as provided by Sigma-Aldrich.

Calibration of LSSmClophensor: Spectroscopy of the Protein Solution

Imaging was performed on the buffered protein solution at given temperature, pH, and Cl$^-$ concentration under the two-photon microscope under conditions similar to those in the in vivo experiments. The efficiency of the photomultiplier tubes of the two detection channels was checked periodically by imaging a control solution. The calibration was performed on a series of solutions at a fixed pH and temperature and containing different Cl$^-$ concentrations. By means of Eq. **11**, we first computed the apparent K_d for Cl$^-$ at the specified pH. Then, by substituting into Eq. **10**, we obtained the pK_a. Having fixed the pK_a we finally fitted Eq. **9** on the pH calibration data, and thus, we obtained the asymptotic values θ_L and θ_R and the term a. The term r(0) was derived directly from the spectra corrected for bleed through. Table S1 shows the values and errors of the parameters used in this study, and Fig. S2 shows the effect of temperature on the spectra at pH values of 6 and 8 and on the fitting parameters pK_a and R_0.

Absence of Intramolecular FRET in LSSmClopHensor

Our data prove that there is no FRET between E^{2}GFP and LSSmKate2 as shown by the following argument. The bleed-through coefficients were measured in solutions of the two proteins separately, and therefore, they cannot account for FRET occurring in the complete sensor. If there were any intramolecular transfers of energy from E^{2}GFP to LSSmKate2, the excitation spectra measured in

the red channel after bleed-through correction (Fig. 1*B*) would show some dependency on pH. Fig. 1*B* shows that the residues of LSSmKate2 excitation spectra, computed as the difference of the spectra measured at a given pH and the spectra averaged on 10 different values of pH, are independent on pH. This shows that there is no detectable FRET from E^{2}GFP to LSSmKate2.

In Utero Electroporation

Tripolar in utero electroporation targeting pyramidal neurons of the visual cortex was performed as previously described (30, 61). Timed pregnant CD1 mice (strain code 022; Charles River) were anesthetized at E15.5 with isoflurane (induction, 4%; surgery, 2%), and the uterine horns were exposed by laparotomy. Expression vectors (1–3 μg/μL in water) and Fast Green dye (0.3 μg/μL; Sigma-Aldrich) were injected (5–6 μL) through the uterine wall into one of the embryo's lateral ventricles by a 30-gauge needle. While the embryo's head was carefully held between standard forceps-type circular electrodes (5-mm diameter; negative poles; Nepa Gene), a third electrode (5 × 3 mm; positive pole) was positioned on the back of the head. Six electrical pulses (amplitude, 30 V; duration, 50 ms; intervals, 1 s) were delivered with a square-wave generator (CUY21EDIT; Nepa Gene or BTX ECM 830; Harvard Bioscience). The uterine horns were returned into the abdominal cavity, and embryos continued their normal development until delivery.

HEK293T Cell Cultures

HEK293T cells were cultured in DMEM supplemented with 1 mM sodium pyruvate, 2 mM L-glutamine, 100 U/mL penicillin, 100 μg/mL streptomycin, 10% FBS, and 10 mM Hepes. Cells were transfected with the Effectene transfection reagent (catalog no. 301425; Qiagen).

Minimization of the Sum of the Fit Residues

The residue defined as

$$R = \sum_{i=1}^{n} \left(G_{*_{pH}}(\lambda_i) - \left(\delta G_{*_{6.0}}(\lambda_i) + \varepsilon G_{*_{8.0}}(\lambda_i) \right) \right)^2 \qquad \textbf{[S1]}$$

is a quadratic function of δ and ε, and it defines a paraboloid. Its minimum can be found in correspondence of the zero of the partial derivative of R in respect of δ and ε:

$$\begin{cases} \dfrac{\partial R}{\partial \delta} = 0 \\[2mm] \dfrac{\partial R}{\partial \varepsilon} = 0 \end{cases}. \qquad \textbf{[S2]}$$

Since R is quadratic, the system is linear and can be easily solved, returning two analytical expressions for δ and ε:

$$\delta = \frac{\sum_{i=1}^{n} G_{*_{8.0}}(\lambda_i)^2 \sum_{i=1}^{n} G_{*_{6.0}}(\lambda_i) - \sum_{i=1}^{n} G_{*_{6.0}}(\lambda_i) G_{*_{8.0}}(\lambda_i) \sum_{i=1}^{n} G_{*_{8.0}}(\lambda_i) G_{*_{pH}}(\lambda_i)}{\nabla} \qquad \textbf{[S3]}$$

$$\varepsilon = \frac{\sum_{i=1}^{n} G_{*_{6.0}}(\lambda_i)^2 \sum_{i=1}^{n} G_{*_{8.0}}(\lambda_i) G_{*pH}(\lambda_i) - \sum_{i=1}^{n} G_{*_{6.0}}(\lambda_i) G_{*_{8.0}}(\lambda_i) \sum_{i=1}^{n} G_{*_{6.0}}(\lambda_i) G_{*_{pH}}(\lambda_i)}{\nabla}, \qquad \textbf{[S4]}$$

where the term ∇ is defined as

$$\nabla = \sum_{i=1}^{n} G_{*_{8.0}}(\lambda_i)^2 \sum_{i=1}^{n} G_{*_{6.0}}(\lambda_i)^2 - \left(\sum_{i=1}^{n} G_{*_{6.0}}(\lambda_i) G_{*_{8.0}}(\lambda_i) \right)^2. \qquad \textbf{[S5]}$$

Statistical Handling of Data and Error Propagation

Cells were screened before analysis and were excluded if the red signal was equal to or lower than twice the offset signal. The fluorescence recorded in each pixel is affected by random fluctuations of the laser power and by shot noise. These noise sources are superimposed on the actual signal, introducing an uncertainty on the spectral measures, which ends up as an error on the pH and chloride estimates. The error present at each pixel of the pH and chloride maps can be quantified by the quality of the fit attained when projecting the pixel spectra on the calibration spectra obtained at pH 6 and 8. The uncertainty of the fit of the spectra is given by

$$\sigma = \sqrt{\frac{R}{n-2}}, \qquad \textbf{[S6]}$$

where R is the sum of the fit residues (Eq. **S1**), and n is the number of wavelengths. The normalization factor is given by n − 2, which is the number of dfs of the system having obtained two parameters from the fit. With only two wavelengths, the residue is zero, and it is impossible to estimate the fit error. The uncertainty σ can be partitioned on the two components, obtaining two expressions for the contribution of each component to the total residue plus a term representing the covariance of the two components:

$$\sigma_\varepsilon^2 = \sigma^2 \sum_{j=1}^{n} \left(\frac{\partial \varepsilon}{\partial G_{*pH}(\lambda_j)} \right)^2 = \sigma^2 \frac{\sum_{i=1}^{n} G_{*6.0}(\lambda_i)^2}{\nabla} \qquad \text{[S7]}$$

$$\sigma_\delta^2 = \sigma^2 \sum_{j=1}^{n} \left(\frac{\partial \delta}{\partial G_{*pH}(\lambda_j)} \right)^2 = \sigma^2 \frac{\sum_{i=1}^{n} G_{*8.0}(\lambda_i)^2}{\nabla} \qquad \text{[S8]}$$

$$\sigma_{\delta\varepsilon} = \sigma^2 \sum_{j=1}^{n} \left(\frac{\partial \varepsilon}{\partial G_{*pH}(\lambda_j)} \frac{\partial \delta}{\partial G_{*pH}(\lambda_j)} \right) = -\sigma^2 \frac{\sum_{i=1}^{n} G_{*6.0}(\lambda_i) G_{*8.0}(\lambda_i)}{\nabla}. \qquad \text{[S9]}$$

As an example, we explicitly compute Eq. **S8**:

$$\sigma_\varepsilon^2 = \sigma^2 \sum_{j=1}^{n} \left(\frac{\partial \varepsilon}{\partial G_{*pH}(\lambda_j)} \right)^2 = \sigma^2 \sum_{j=1}^{n} \left(\frac{\partial}{\partial G_{*pH}(\lambda_j)} \frac{\sum_i G_{*6.0}(\lambda_i)^2 \sum_i G_{*8.0}(\lambda_i) G_{pH}(\lambda_i) - \sum_i G_{*6.0}(\lambda_i) G_{*8.0}(\lambda_i) \sum_i G_{*6.0}(\lambda_i) G_{pH}(\lambda_i)}{\nabla} \right)^2,$$

where it is implicit that the summations over i run from one to n. Since ∇ does not contain $G_{*pH}(\lambda_j)$ and given that the only nonzero terms of the summation containing $G_{*pH}(\lambda_i)$ are the terms where i = j, we obtain the following expression:

$$\sigma_\varepsilon^2 = \sigma^2 \sum_{j=1}^{n} \left(\frac{\sum_{i=1}^{n} G_{*6.0}(\lambda_i)^2 G_{*8.0}(\lambda_j) - \sum_{i=1}^{n} G_{*6.0}(\lambda_i) G_{*8.0}(\lambda_i) G_{*6.0}(\lambda_j)}{\nabla} \right)^2, \qquad \text{[S10]}$$

which can be further expanded:

$$\sigma_\varepsilon^2 = \sigma^2 \frac{\left(\sum_{i=1}^{n} G_{*6.0}(\lambda_i)^2 \right)^2 \sum_{i=1}^{n} G_{*8.0}(\lambda_i)^2 + \left(\sum_{i=1}^{n} G_{*6.0}(\lambda_i) G_{*8.0}(\lambda_i) \right)^2 \sum_{i=1}^{n} G_{*6.0}(\lambda_i)^2}{\nabla^2} -$$

$$\frac{2 \sum_{i=1}^{n} G_{*6.0}(\lambda_i)^2 \sum_{i=1}^{n} G_{*6.0}(\lambda_i) G_{*8.0}(\lambda_i) \sum_{i=1}^{n} G_{*6.0}(\lambda_j) G_{*8.0}(\lambda_j)}{\nabla^2}.$$

Since the summations are decoupled, the indexes j and i are interchangeable. Furthermore, the expansion of ∇ (Eq. **S5**) returns

$$\sigma_\varepsilon^2 = \sigma^2 \frac{\sum_{i=1}^{n} G_{*6.0}(\lambda_i)^2 \left[\sum_{i=1}^{n} G_{*8.0}(\lambda_i)^2 \sum_{i=1}^{n} G_{*6.0}(\lambda_i)^2 - \left(\sum_{i=1}^{n} G_{*6.0}(\lambda_i) G_{*8.0}(\lambda_i) \right)^2 \right]}{\left[\sum_{i=1}^{n} G_{*8.0}(\lambda_i)^2 \sum_{i=1}^{n} G_{*6.0}(\lambda_i)^2 - \left(\sum_{i=1}^{n} G_{*6.0}(\lambda_i) G_{*8.0}(\lambda_i) \right)^2 \right]^2}$$

$$\qquad \text{[S11]}$$

$$\sigma_\varepsilon^2 = \sigma^2 \frac{\sum_{i=1}^{n} G_{*6.0}(\lambda_i)^2}{\nabla}.$$

The term $\sigma_{\delta\varepsilon}$ (Eq. **S9**) is caused by the fact that there is a reciprocal dependence between the components δ and ε, and therefore, their covariance is nonzero.

The first step of the propagation of these uncertainties is the computation of their effect on the angle θ defining the pH value (Fig. 1*C*). The angle θ is a nonlinear function of δ and ε:

$$\theta = \text{atan} \frac{\varepsilon}{\delta}. \qquad \text{[S12]}$$

The uncertainty on θ can be computed from its first-order Taylor expansion:

$$\Delta\theta^2 = \left| \frac{\partial\theta}{\partial\varepsilon} \right|^2 \sigma_\varepsilon^2 + \left| \frac{\partial\theta}{\partial\delta} \right|^2 \sigma_\delta^2 + 2 \frac{\partial\theta}{\partial\varepsilon} \frac{\partial\theta}{\partial\delta} \sigma_{\delta\varepsilon}. \qquad \text{[S13]}$$

The first two terms account for the propagation of the errors on δ and ε, while the third term accounts for their covariance. Given that $(d/dx)\tan(x) = (1/1 + x^2)$ from Eq. **S13**, we obtain

$$\Delta\theta^2 = \left(\frac{\delta^2}{\varepsilon^2 + \delta^2}\right)^2 \left(\frac{1}{\delta^2}\sigma_\varepsilon^2 + \frac{\varepsilon^2}{\delta^4}\sigma_\delta^2 - 2\frac{\varepsilon}{\delta^3}\sigma_{\delta\varepsilon}\right).$$ [S14]

After simplifications and conversion of θ from radians to degrees, we obtain

$$\Delta\theta = \frac{180}{3.14}\frac{\sqrt{\delta^2\sigma_\varepsilon^2 + \varepsilon^2\sigma_\delta^2 - 2\delta\varepsilon\sigma_{\delta\varepsilon}}}{(\varepsilon^2 + \delta^2)}.$$ [S15]

Finally, Δθ can be expressed in function of the uncertainty of δ and ε and of their covariance by substituting Eqs. **S7–S9** into Eq. **S15**, yielding

$$\Delta\theta = \frac{180}{3.14}\frac{\sigma_y}{(\varepsilon^2 + \delta^2)}\sqrt{\frac{\delta^2\sum_{i=1}^{n}G_{*6.0}(\lambda_i)^2 + \varepsilon^2\sum_{i=1}^{n}G_{*8.0}(\lambda_i)^2 + 2\delta\varepsilon\sum_{i=1}^{n}G_{*6.0}(\lambda_i)G_{*8.0}(\lambda_i)}{\sum_{i=1}^{n}G_{*8.0}(\lambda_i)^2\sum_{i=1}^{n}G_{*6.0}(\lambda_i)^2 - \left(\sum_{i=1}^{n}G_{*6.0}(\lambda_i)G_{*8.0}(\lambda_i)\right)^2}}.$$ [S16]

This expression can be used to compute the uncertainty on pH. Indeed, by inverting Eq. **9**, we express the pH as a function of θ and of the parameters obtained during the calibration procedure (Table S1):

$$pH = pK_a + \frac{1}{a}\log_{10}\left(\frac{\theta - \theta_L}{\theta_R - \theta}\right).$$ [S17]

The uncertainty on pH can be computed as a function of the uncertainty on the fitting parameters θ_L, θ_R, a, and pK_a (reported in Table S1) and of the uncertainty on θ:

$$\Delta pH^2 = \Delta pK_a^2 + \frac{1}{a^4}\Delta a^2\left[\log_{10}\left(\frac{\theta - \theta_L}{\theta_R - \theta}\right)\right]^2 + 2.302\frac{1}{a^2}\left[\frac{\Delta\theta_L^2}{(\theta - \theta_L)^2} + \frac{\Delta\theta_R^2}{(\theta_R - \theta)^2} + \frac{\Delta\theta^2(\theta_R - \theta_L)^2}{(\theta_R - \theta)^2(\theta - \theta_L)^2}\right].$$ [S18]

The error on the chloride measure was computed as follows. We calculated the uncertainty on K_d^{Cl} by combining Eqs. **9** and **10** and by differentiating the resulting equation. The error on K_d^{Cl} depends on the uncertainty of pK_a (calculated from the fit of Fig. S2B; reported in Table S1) and on the uncertainty of the error of pH:

$$\Delta K_d^{Cl} = \left(13.1 \cdot 2.30 \cdot 10^{pH - pK_a}\right)\sqrt{\Delta pH^2 + \Delta pK_a^2}.$$ [S19]

Finally, the error on the chloride concentration was computed by propagating the errors on K_d^{Cl} and on r(0) as obtained from the chloride calibration (Table S1):

$$\Delta Cl = \sqrt{\left[\left(\frac{r(0)}{r(Cl)} - 1\right)\Delta K_d^{Cl}\right]^2 + \left[\left(\frac{K_d^{Cl}}{r(Cl)}\right)\Delta r(0)\right]^2}.$$ [S20]

For each cell, we computed the mean pH and chloride values by averaging the pH and chloride estimates of each pixel weighted for the square of the relative error:

$$pH = \frac{\sum_{i=1}^{m}\frac{1}{\Delta pH_i^2}pH_i}{\sum_{i=1}^{m}\frac{1}{\Delta pH_i^2}},$$ [S21]

where m is the number of pixels in the cell profile, and

$$Cl = \frac{\sum_{i=1}^{m}\frac{1}{\Delta Cl_i^2}Cl_i}{\sum_{i=1}^{m}\frac{1}{\Delta Cl_i^2}}.$$ [S22]

For each cell, the error on the weighted pH and chloride values is computed as the mean of the errors of each pixel. Alternatively, pH and chloride values were computed by averaging the fluorescence on the entire cell body profile, while errors were computed as outlined above. The two methods gave similar results.

Determination of Extinction in Vivo

We imaged HEK293T cells transfected with a YFP plasmid (pEYFP-N1; Clontech) to determine the relative distribution of fluorescence in our G and R detectors in the absence of wavelength-dependent extinction. To determine the differential extinction of emitted fluorescence in vivo, we acquired Z stacks down to a depth of 350 μm with a step size of 1 μm in YFP-expressing mouse cortical neurons (35). In all of these experiments, the excitation wavelength was set at 960 nm.

For the determination of the effects of scattering and absorption on excitation, we measured the two-photon excitation spectra of YFP expressed in HEK293T (zero scattering reference) or in the mouse cortex at various depths (34). Spectra were obtained by acquiring sets of images in the wavelength range 900–1,000 nm. Shorter wavelengths (800–900 nm) were not explored because of the low fluorescence yield of YFP in this range.

Ideally, the fluorescent protein used to probe the coupling between excitation scattering/absorption and extinction of emission should have exactly the same emission spectra of the combination of E²GFP and LSSmKate2. YFP did not satisfy this condition; however, the different power distribution of fluorescence of YFP in the red channel compared with LSSmKate2 caused only a minor effect on the extinction estimate as shown by the following argument. The power distribution of a fluorophore within a bandpass filter can be computed by the emission spectra. If we assume that the bandpass filter has a rectangular profile, we can compute the mean emission wavelength of a fluorophore in the filter bandwidth as

$$\lambda_{mean} = \frac{\int_{\lambda_{left}}^{\lambda_{right}} F(\lambda)\lambda d\lambda}{\int_{\lambda_{left}}^{\lambda_{right}} F(\lambda)d\lambda},$$

[S23]

where λ_{left} and λ_{right} are the limits of the bandpass filters, and $F(\lambda)$ is the fluorescence of each fluorophore. As shown in Fig. S5, the mean wavelength of the emission of LSSmKate2 in the red channel (606 nm) is shifted 7 nm toward the red in comparison with YFP (599 nm). The distance between the LSSmKate2 mean wavelength and the mean wavelength of YFP/E²GFP measured in the green channel (531 nm) is 75 nm. That means that the difference in mean wavelengths between YFP and LSSmKate2 in the red channel is only about 9% of the distance between the spectral windows, thus leading to a relatively small error in the estimate of the correction factor.

Intracellular Stoichiometry of LSSmClopHensor: Fluorescence Recovery After Photobleaching Measurements

We performed two independent controls of the sensor's protein component stoichiometry within cells based on in vivo fluorescence recovery after photobleaching (FRAP) and on the measure of the correlation spectra of fluorescence fluctuations. We reasoned that, if the sensor is present in neurons as a correctly formed fusion protein, its molecular mass (about 54 kDa) approaches the limit for free diffusion through nuclear pores (62). Thus, we bleached the sensor fluorescence in the nucleus, and we imaged the recovery process by in vivo two-photon imaging. The rate of recovery provides an estimate of the diffusion speed of the fluorescent molecules between the bleached volume and the remaining cell volume. In these experiments, we focused the laser power (80 mW measured at the objective lens) for 15 s onto one point inside the nucleus to photobleach the nuclear fluorescent proteins (bleach). Then, we measured the recovery of the nuclear fluorescence until recovery was completed. The recovery of fluorescence is caused by the ongoing exchange of sensor molecules between the nuclear compartment and the cytosol, and it is described by an exponential growth with a time constant, which depends on the rate of diffusion through the nuclear membrane (62). The recovery process is provided by the following function:

$$I(t) = \frac{S_{Nucl}}{S_{Nucl} + S_{Cyt_{(t)}}} = \left(I_\infty - I_{post}\right)\left(1 - e^{-\frac{t}{\tau}}\right) + I_{post},$$

[S24]

where S_{Nucl} is the integrated fluorescence measured in the nucleus, and S_{Cyt} is the integrated fluorescence measured in the cytoplasm. I_∞ and I_{post} are the normalized fluorescence intensities measured at the asymptote and at the beginning of the recovery, respectively; τ is the time constant of the shuttling between nucleus and cytoplasm. To explore this process at different timescales and minimize bleaching during imaging, in each FRAP experiment, the frame period was gradually increased from 30 s (initial recovery) to 60 and 120 s toward the asymptote. The power used for imaging during recovery depended on the protein expression level but was always under 20 mW (measured at the objective lens).

Since fluorescent proteins are not enrolled in active translocation through the nuclear membrane, the time course of the fluorescence recovery strongly depends on the molecular weight of the protein itself. If LSSmClopHensor is present as a correctly formed fusion between LSSmKate2 and E²GFP, the time course of the recovery of fluorescence should be much slower than the recovery of YFP. Experimental testing of this assumption was performed in vivo in pyramidal neurons expressing either LSSmKate2 or YFP (line H in ref. 35), and the time course of the fluorescence recovery is shown in Fig. S3A. The time constant of the recovery measured in the cells examined, >12 min, was consistent with previous measurements on GFP dimers (63). This rate was very slow compared with the rate of fluorescence recovery of a YFP monomer, which was in the 2- to 4-min range (Fig. S3A).

Intracellular Stoichiometry of LSSmClopHensor: Fluorescence Correlation Spectroscopy

We exploited the fact that fluorescence correlation spectroscopy can be used to count the number of fluorescent particles in the focal volume. This technique can be used to estimate the numbers of E²GFP and LSSmKate2 molecules, thus allowing us to estimate their stoichiometry (Fig. S3B). Here, it should be kept in mind that increasing [Cl⁻]$_i$ leads to a progressive quenching of E²GFP fluorescence, which will decrease the number of active particles in the G channel. Accordingly, Fig. S3B shows that, with diminishing Cl⁻, the apparent stoichiometry approaches asymptotically a 1:1 ratio, consistent with a stable fusion protein and with perfect pairing between E²GFP and LSSmKate2. The comparison of the active molecules in the R and G channels provides the stoichiometry of the sensor. Since this technique is based on light fluctuation inside the point-spread function of excitation, the lower the protein concentration is

inside the cell, the more accurate the measure of the number of fluorescent protein molecules. Thus, we transfected cells with a reduced concentration of plasmidic DNA (100 ng for a 60-mm cell plate). The measurement was made 5 d after transfection to make sure that both green and red protein expression have reached steady state. Our results (Fig. S3B) showed that, in the absence of chloride, the rate of fluctuations in the two channels tended to one, consistently with a perfect pairing between E^2GFP and LSSmKate2.

HEK293T cells were washed three times for 3 min each with a pH 7.0 buffer solution (20 mM Hepes, 0.6 mM $MgSO_4$, 38 mM sodium gluconate, 100 mM potassium gluconate) containing a mix of ionophores as previously described, and extracellular chloride was varied by adding NaCl to the buffered medium. We set a gradually increasing chloride concentration of the buffer medium (0, 7, 10, 20, 45, 70, 85, 95, 120, 160, 270, and 400 mM). Measurements were performed with a 60× water immersion objective on a Leica sp2 system, with excitation at 458 nm: this wavelength excites both the isosbestic point for E^2GFP and the LSSmKate2 at its excitation peak. We used two avalanche diodes in the detection channels. The signal was sent to a two-channel counting board (model M9003; Hamamatsu Photonics K.K.) and analyzed with its proprietary software (U9451; Hamamatsu Photonics K.K.). We used low excitation power to avoid artifacts caused by E^2GFP molecules escaping to dark states. The number of optically active protein molecules given by a fluorescence correlation spectroscopy measurement is inversely proportional to the magnitude of the autocorrelation function of the fluorescence of that protein. Therefore, E^2GFP autocorrelation gives the number of E^2GFP molecules. To this end, we selected E^2GFP fluorescence by a 500- to 550-nm bandpass filter, and the fluorescence was split and sent to the two diodes. This configuration is necessary to avoid after-pulse rebound in the detectors. The same procedure was followed for the LSSmKate2 fluorescence by using a 575- to 640-nm bandpass filter.

FLIM

We measured the fluorescence lifetime of LSSmClopHensor as an alternative method to estimate pH_i, since this approach is independent of excitation distortion. We show that the fluorescence lifetimes of the protonated and deprotonated forms of E^2GFP are different. Fig. S6A shows the fluorescence decay of the sensor excited at 910 nm and imaged in HEK cells. At this wavelength, we measured a mix of the protonated and deprotonated lifetimes, yielding a relationship between the time course of fluorescence decay and pH. We obtained a calibration curve of pH vs. lifetime both in protein solution and in HEK cells (Fig. S6B). We acquired the spectra of E^2GFP and LSSmKate2 in P18 pyramidal neurons in vivo for the spectroscopic computation of pH_i, and afterward, we measured the fluorescence decay at 910 nm (Fig. S6 C and D). In this way, we estimated the pH_i of each imaged cell ($n = 11$) by two independent methods, only one of which was affected by tissue absorption (Fig. S6E). Fig. S6F shows an excellent agreement of the two pH_i measurements: pH_i 7.15 ± 0.07 and 7.17 ± 0.06 for the spectroscopic and FLIM measurements, respectively.

Since the protonated and deprotonated states of E^2GFP have different fluorescence lifetimes, measurements of pH based on lifetime are independent from excitation/emission light extinction. FLIM measurements were performed by using a time-to-digital converter board (model SPC-830; Becker & Hickl GmbH) that was synchronized to the two-photon laser with a fast diode detector (pulse period of 12.5 ns). The voltage of the photomultipliers of the Prairie Microscope was maintained constant (900 V) for both calibration and in vivo experiments. The instrument response function (IRF) was measured at the same photomultiplier voltage by using KH_2PO_4 microcrystals, which convert the IR light of the laser into visible light by second harmonic generation.

Lifetime measurements were calibrated both in purified protein buffered to a known pH level and in cells by using the same pH buffers supplied with ionophores as described above. As expected from literature, we found that lifetimes measured in cells were slightly shifted with respect to the ones measured in solutions of purified protein at the same pH. This can be explained by the effect of the viscosity of the intracellular medium on the lifetime of the fluorescence of our GFP mutant (60).

Lifetime images were acquired with the Prairie Ultima system by synchronizing the microscope galvos to the Becker & Hickl GmbH software by using open source hardware (Arduino Uno). The acquisition of each FLIM image required about 2 min. The power of the laser beam at the objective was set under 5 mW, and the wavelength was set to 910 nm. After each acquisition was completed, the measurement was repeated with the laser switched off for the acquisition of the dark image. In brief, FLIM acquisition and analysis were performed as follows.

i) Lifetime images and dark images were imported in ImageJ by using the Bio-Formats plugin. The imported files are xyt matrices that contain both spatial and temporal decay information.
ii) The dark xyt matrix was subtracted from the xyt lifetime matrix (dark subtraction).
iii) A region of interest (ROI) was drawn for each cell, and the mean value of fluorescence of each image was calculated.
iv) Lifetime decays for each function were exported in Origin and fitted with a single exponential convoluted with the measured IRF function:

$$I(t) = \int\limits_{-\infty}^{+\infty} Ae^{-\frac{t-t'-t_0}{\tau}} \, IRF(t') \, dt'. \tag{S25}$$

The different parts of the imaged field experience a slight shift in the timing of the excitation, likely owing to slight differences in the optical paths: this was accounted for with the free parameter t_0 ($t_0 \sim 1$ ns).

v) The measured lifetime was converted to pH using the calibration dataset (Fig. S6B).

Workflow of Calibration and Processing of Imaging Data

Images were analyzed with ImageJ (https://imagej.nih.gov/ij/). The images were processed as follows.

i) Dark subtraction. Dark images were acquired in both G and R channels, with the excitation beam switched off to record the signal offset. Since the dark image from a scanning microscope does not contain any spatial structure (as opposed to what happens with a

CCD or complementary metal-oxide semiconductor sensor), the dark image was averaged, and the mean value was subtracted from imaging data.

ii) Flat correction. Regardless of the quality of alignment of the optic bench and the illumination of the imaging field, it is never uniform, and it varies with excitation wavelength. To compensate for this, we acquired a library of flat-field images that were dark subtracted, normalized to a mean value of one, and used to correct the imaging data. For each wavelength, the flat is an image obtained by the mean of 50 frames of a solution of a broadband emitting fluorophore (Rhodamine 6G; 1 μM) loaded in the spectroscopy chamber. Imaging data were, therefore, calibrated following the equation:

$$\mathbf{I}_{cal} = \frac{(\mathbf{I}_{raw} - dark)}{F}, \qquad \text{[S26]}$$

where *dark* is the mean dark signal, and *F* is the dark-subtracted flat-field image obtained at the same excitation wavelength and at the same scanning zoom (bold letters indicate images rather than scalars). The ratio is computed pixel by pixel. We verified that it was critical to obtain a new flat library each time that the optic bench was realigned. We noticed that the relative gain of the two acquisition channels was subject to small changes from one imaging session to the other. Of course, these changes would affect both the chloride measure and the estimate of the correction for the emission in the G and R channels. The flat data are also used to correct for changes in the relative gain of the two detection channels.

iii) Normalization of each image to the square of the number of photons on the sample (since two-photon fluorescence is quadratic with photon number).

iv) Alignment of the images for random translations occurring during the acquisition because of motion artifacts using the Stackreg or Template Matching plugins of ImageJ.

v) Design of an ROI for each cell and measurement of the mean intensity at each wavelength. For each cell in each optical section, we obtained a spectral series that was analyzed by custom software that implements the computation pipeline described. Alternatively, we developed an ImageJ macro that computes the maps of both pH_i and $[Cl^-]_I$, applying the equations described in *Materials and Methods*.

## Effect of Laser Power Stability on pH and Cl⁻ Estimates

Laser fluctuations are a main source of noise in all imaging measures, and this problem is especially severe in nonratiometric imaging, such as Ca^{2+} imaging based on Oregon Green and the GCaMP family of indicators. In single-excitation ratiometric measurements, the problem is largely solved by the presence of a reference channel. Thus, our ratiometric measurements of chloride are insensitive to laser fluctuations, since they are obtained by taking the ratio of the fluorescence from the G and R channels at a fixed excitation wavelength. However, fluctuations of laser power occurring between frames acquired at different excitation wavelengths affect the determination of pH that relies on spectral data. Since the K_d for Cl depends on pH, fluctuations occurring during the acquisition of spectra also affect indirectly the determination of Cl⁻. To ensure uniformity, the power at the microscope entry port was controlled before each spectroscopic measurement by the electronics described elsewhere (33). One advantage of the spectroscopic method is that, since it relies on fitting the experimental data with the calibration curves at several wavelengths, errors caused by laser fluctuations (or other sources) at a given wavelength are attenuated by the fitting process. Finally, since the residue is used to compute the indetermination of pH and Cl, any error affecting the regularity of the spectra ends up in the errors of the pH and Cl estimates. Therefore, although it is unlikely to compensate perfectly for laser fluctuations, it is possible to provide a statistically meaningful estimate of the measurement errors, which include the impact of laser fluctuations. The situation relative to dynamic imaging is more complex. Since in these experiments, we alternate only two wavelengths, pH is obtained by an exact solution, and thus, we cannot estimate the error by propagating the residue value. In this case, we use the red signal as a measure of the relative intensity of the beams at the two wavelengths by normalizing the E^2GFP signal to the LSSmKate2 signal. The correction of the fluorescence red shift was obtained before obtaining the temporal series by means of a complete steady-state spectra. Finally, to reduce the impact of pH error on chloride measurements, the time series of pH values were smoothed by a rectangular box filter before computing chloride affinity.

LFP Recordings

A thick-wall borosilicate micropipette with filament (1 mm o.d., 0.58 mm i.d.) was pulled to a tip diameter of about 1.5 μm (resistance about 2 MΩ when filled with saline solution) and connected to a voltage amplifier by means of a high-impedance head stage (EXT-02F; NPI Electronics). The electrode was inserted in the cortex through a perforated coverslip to a depth of about 250 μm. The reference electrode was an Ag/AgCl pellet immersed in saline outside of the skull in the immediate proximity of the craniotomy. The extracellular potential was amplified 1,000-fold, band pass filtered (0.1–1,000 Hz), and oversampled at 5–10 kHz by an NI-usb6251 acquisition board. Acquisition and analysis was performed through custom software written in MatLab that exploits the Chronux toolbox for spectral analysis (chronux.org/).
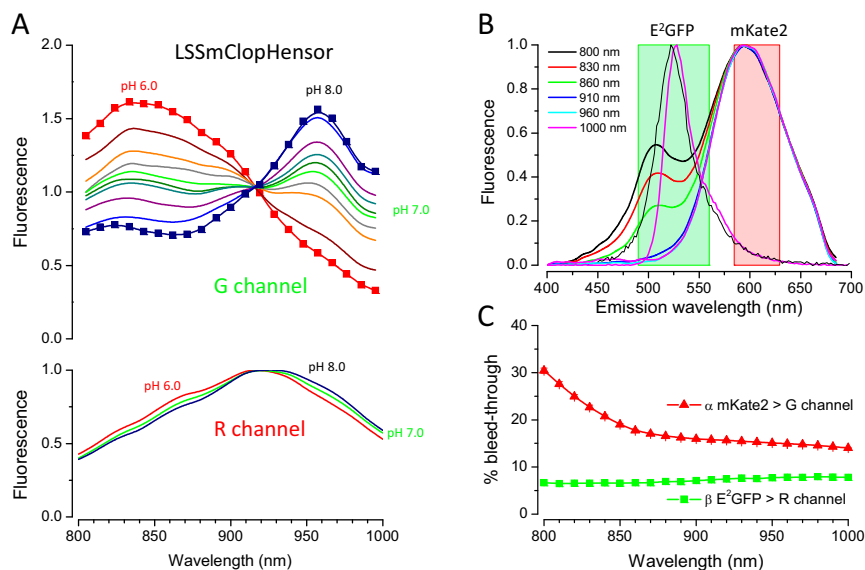
Fig. S1. Raw excitation spectra of LSSmClopHensor and fluorescence bleed through between the acquisition channels. (*A*) Spectra have been obtained from purified protein in aqueous solution imaged under the two-photon microscope. Data have been normalized at the value of the red fluorescence at 910 nm. The red fluorescence showed an apparent dependency on pH. The symbols indicate the wavelengths at which the spectra have been sampled, and they have been omitted in most traces for clarity. The nonlabeled spectra of LSSmClopHensor have been obtained at pH values of 6.4, 6.8, 6.9, 7.0, 7.1, 7.2, 7.4, and 7.6. (*B*) Emission spectra of E²GFP and LSSmKate2 depend on the wavelength of two-photon excitation. The green and red rectangles show the bandwidth of the emission filters of our imaging setup (G: 525/70 nm; R: 607/45 nm). E²GFP shows only a modest change of the emission spectrum, which falls mostly inside the G detection channel. For clarity, only the extremes of the spectra (excitation 800 and 1,000 nm) are shown. In contrast, LSSmKate2 shows a drastic increase of fluorescence emitted in the G detection channel for wavelength shorter than 850 nm. (*C*) The bleed-through coefficients α and β have been derived by measuring the fluorescence of each protein in the green and red channels. As expected from the emission spectra, β is quite constant, while α has a strong dependency on excitation below 850 nm.
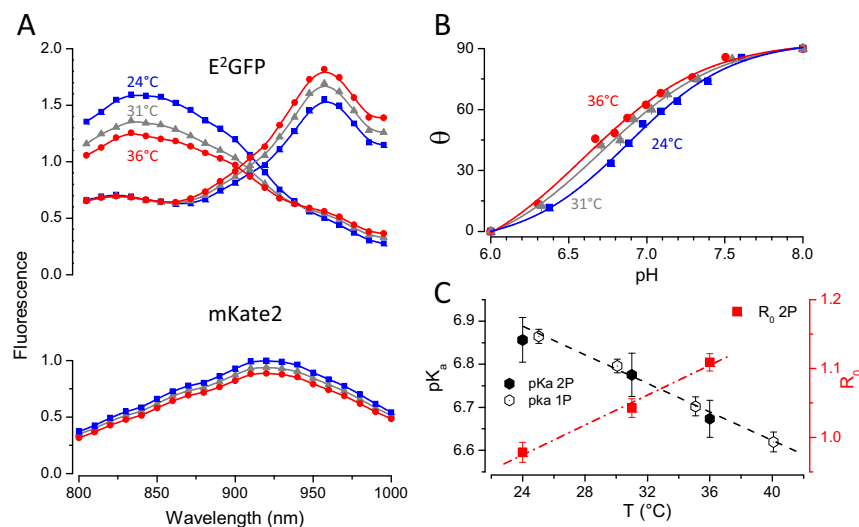

Fig. S2. Dependency of LSSmClopHensor calibration on temperature. (*A*) Excitation spectra at pH 6.0 and 8.0 (peaks at about 840 and 960 nm, respectively) for three different temperatures as indicated in the labels. Notably, the temperature dependency is different for the protonated and deprotonated spectra. The LSSmKate2 spectra experience a slight fluorescence decrease with increasing temperature. (*B*) Calibration curves for pH at three different temperatures. The parameter θ is computed by the spectral decomposition shown in Fig. 1. (*C*) Dependency of pK_a and R_0 on temperature. The filled and empty black symbols report the pK_a measured at two- and one-photon excitation, respectively.
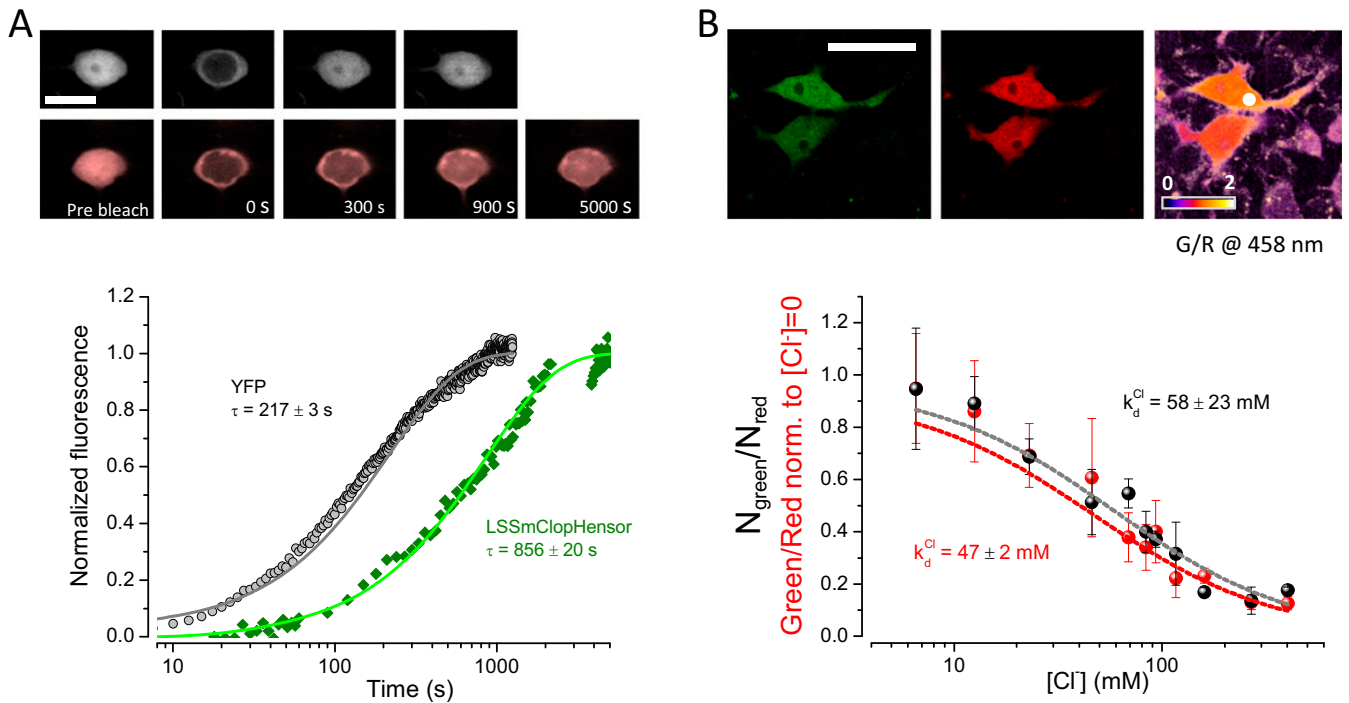
Fig. S3. Molecular integrity of LSSmClopHensor in living cells. (*A*) Nucleus/cytoplasm shuttling of YFP (*Top*) or LSSmClopHensor (*Middle*) in neurons as detected by in vivo FRAP measurements. The first image of each sequence shows the prebleach fluorescence. The recovery images show that the shuttling of LSSmClopHensor is much slower than that of YFP only. *Bottom* shows an example of recovery for YFP and LSSmClopHensor. The recovery of the sensor fluorescence is fitted by a single exponential with a much higher time constant than in the case of YFP, suggesting that most, if not all, LSSmChlophensor molecules are in the dimeric form. (Scale bar: 10 μm.) (*B*) Measure of the relative abundance of E^{2}GFP and LSS mKate2 by means of fluorescence correlation spectroscopy (black) compared with the spectroscopic results (red). HEK cells were imaged while being exposed to increasing concentrations of chloride in the presence of ionophores to allow equilibration of both pH and chloride between the cytosol and the extracellular medium. The pseudocolor image in *Upper* shows the ratio G/R and the location of one fluorescence correlation spectroscopy measurement. *Lower* shows the quantification of the fluorescence correlation spectroscopy measures. The G/R fluorescence ratio (red dots and dashed red fit) is a good estimator of the ratio between the number of optically active green and red proteins, which has been determined by fluorescence correlation spectroscopy. At [Cl$^-$]$_i$ = 0 mM, there is the same number of green and red optically active proteins. (Scale bar: 20 μm.)
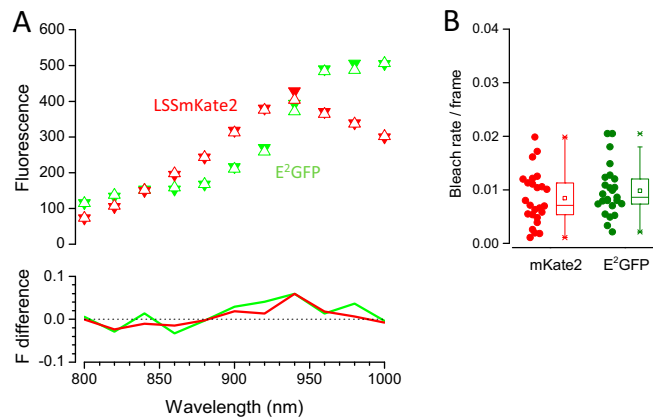

Fig. S4. Effects of bleaching on the spectroscopic measures. (*A*) The repetition of a spectral series on the same cell shows that bleaching was negligible and that the repeatability was equal or better than 96%. Imaging depth was 245 μm, and each spectral dataset was obtained by scanning 11 wavelengths from 800 to 1,000 nm. The green and red symbols show the spectra of E^{2}GFP and LSSmKate2 recorded in two different repeats (empty and filled symbols, respectively). Fluorescence has been corrected for offset, field illumination, and bleed through but not for excitation scattering. (*B*) Bleaching rate measured at 120- to 300-μm depth by means of repeated acquisitions of the same cell bodies. All imaging data shown have been obtained in typical conditions, with 35 mW delivered at the objective output at all wavelengths.
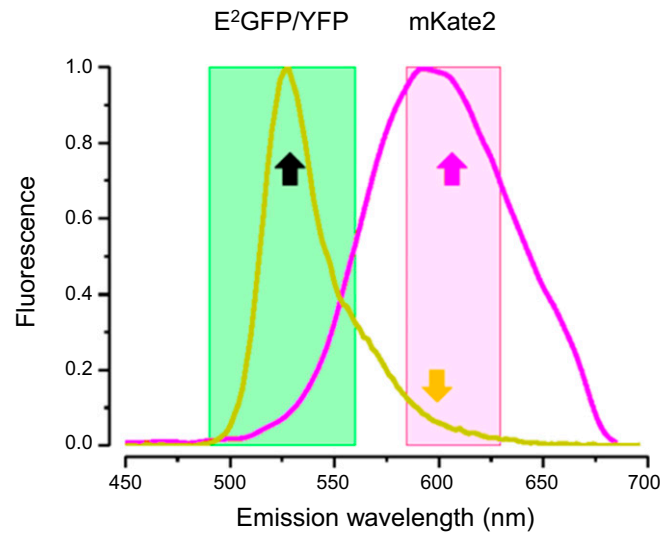
Fig. S5. Comparison of the fluorescence center band in the red channel for YFP and LSSmKate2. Emission spectra of E^{2}GFP/YFP and LSSmKate2 after two-photon excitation at 1,000 nm. The green and magenta rectangles show the bandwidth of the emission filters of our imaging setup (G: 525/70 nm; R: 607/45 nm). The full arrows indicate the mean wavelength emitted by YFP (orange; 599 nm) and LSSmKate2 (magenta; 606 nm) in the red channel. The black arrow indicates the mean wavelength emitted by YFP/E^{2}GFP in the green channel (531 nm).
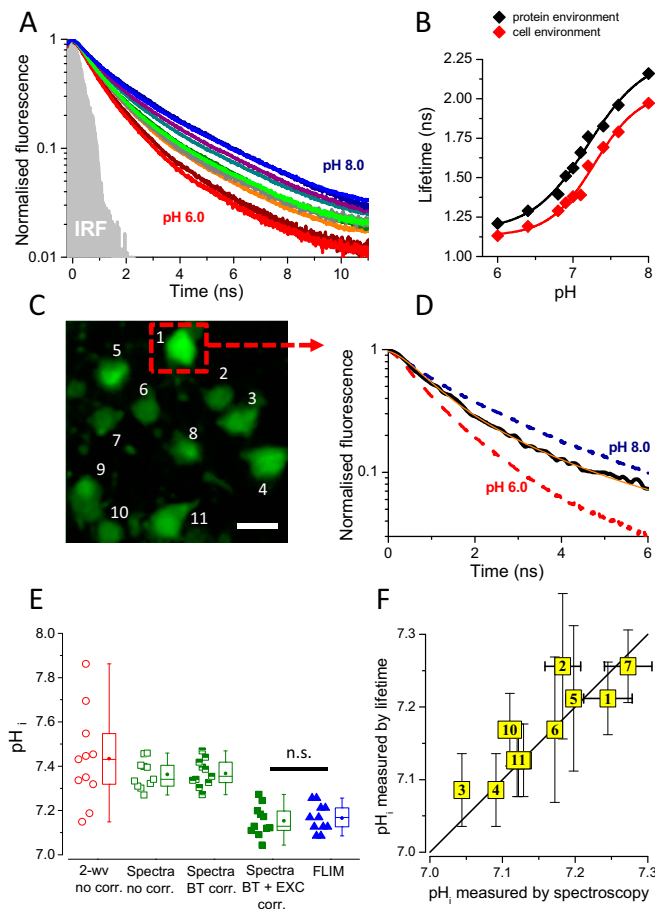
Fig. S6. FLIM of E^{2}GFP was used to measure pH$_i$ in a scattering-independent way and to evaluate the efficacy of the corrections for excitation scattering and intracellular environment. (*A*) FLIM calibration data obtained in HEK cells held in zero chloride and at the specified pH values. For each pH value, at least 30 cells were measured. Fluorescence decay times were measured at pH 6.0, 6.4, 6.8, 6.9, 7.0, 7.1, 7.2, 7.4, 7.6, and 8.0, with corresponding labels omitted for clarity. The distribution of the IRF shows the response of the detectors to a fluorescence pulse. (*B*) Calibration curves showing the average lifetime of E^{2}GFP vs. pH in purified protein solution and in HEK cells, showing a difference because of the different environments. Lifetimes were determined in three different protein samples (black symbols) and in three different cell plates (red symbols). (*C*) Two-photon imaging of a field placed at 150 μm of depth in the cortex of a P18 mouse. pH$_i$ was determined for each labeled neuron by both spectroscopy and FLIM analysis. (Horizontal scale bar: 15 μm.) (*D*) Decay of fluorescence as measured in the boxed neuron in *C* (black line) and its fit (thin orange line). For reference, the fluorescence decays at pH$_i$ 6 and 8 are also shown. (*E*) Comparison of pH$_i$ values for each cell labeled in *C* as obtained from spectroscopy analysis (without and with the different modalities of correction as indicated below the horizontal line) and from lifetime analysis. From the left, pH computed with a conventional ratiometric method with two excitation wavelengths (910 and 960 nm) and no correction for either bleed through or for excitation distortion, pH computed by spectral decomposition without any correction, pH computed by spectral decomposition and correction for bleed through only, and pH$_i$ computed by spectral decomposition and correction for bleed through and excitation distortion. These data have been corrected for the effect of intracellular environment on spectral properties according to Fig. S7*B* (see below). The rightmost dataset shows the pH$_i$ measured by FLIM. The pH$_i$ estimates provided by the spectral method are statistically indistinguishable from the FLIM-based estimates (*P* = 0.36, paired Wilcoxon signed rank test). (*F*) The yellow symbols represent the relationship between the spectroscopic estimate of pH$_i$ (*x* axis) and the FLIM estimate (*y* axis). The plot shows an excellent agreement between the two estimates after the imaging data have been fully corrected for absorption/scattering.
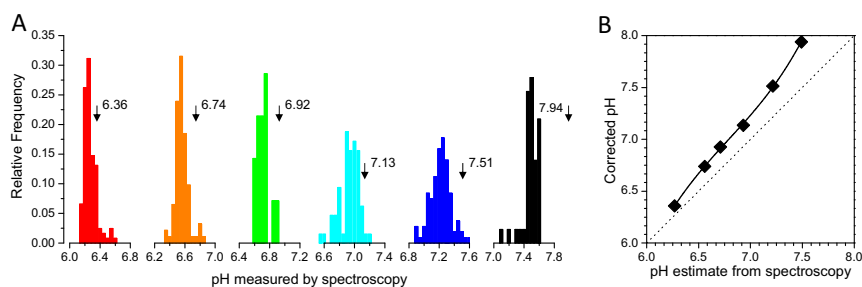
Fig. S7. Calibration of LSSmClopHensor in living cells. (*A*) Effects of intracellular environment on LSSmClopHensor spectroscopy. HEK293T cells were transfected with LSSmClopHensor and imaged in zero chloride solution in the presence of ionophores to allow equilibration of pH between cytosol and extracellular media. Each group of cells was imaged at 31 °C in zero chloride at the pH indicated by the arrow. Each distribution shows the dispersion of the spectroscopic measure of pH_i at a given value of extracellular pH. The comparison of these data with the pH of the extracellular solution (vertical arrows) suggests that the spectroscopic readout performed with the reference spectra is systematically more acidic. This must be because of differences of the sensor optical properties when it is placed in aqueous solution or in the cellular environment. The difference between the observed and the expected pH values is used to produce the transformation that corrects the pH values obtained with the spectra measured in calibration solutions. The figure contains data measured from 704 cells. (*B*) The spectroscopic estimate of pH is shifted toward acidic values and has to be corrected according to the empirical function shown here. Error bars (SE) are contained within the symbol size.

Table S1. Values of the parameters describing LSSmClopHensor dependency on pH and chloride concentration at three different temperatures (*n* = 3 at each temperature)

Parameter	24 °C	31 °C	36 °C
pK_a	6.88 ± 0.05	6.77 ± 0.05	6.67 ± 0.04
θ_L	−6.53 ± 0.16	−8.44 ± 0.24	−12.22 ± 0.24
θ_R	93.34 ± 0.11	92.29 ± 0.12	91.97 ± 0.09
A	1.31 ± 0.01	1.34 ± 0.01	1.30 ± 0.012
r(0)	0.98 ± 0.03	1.04 ± 0.03	1.11 ± 0.03